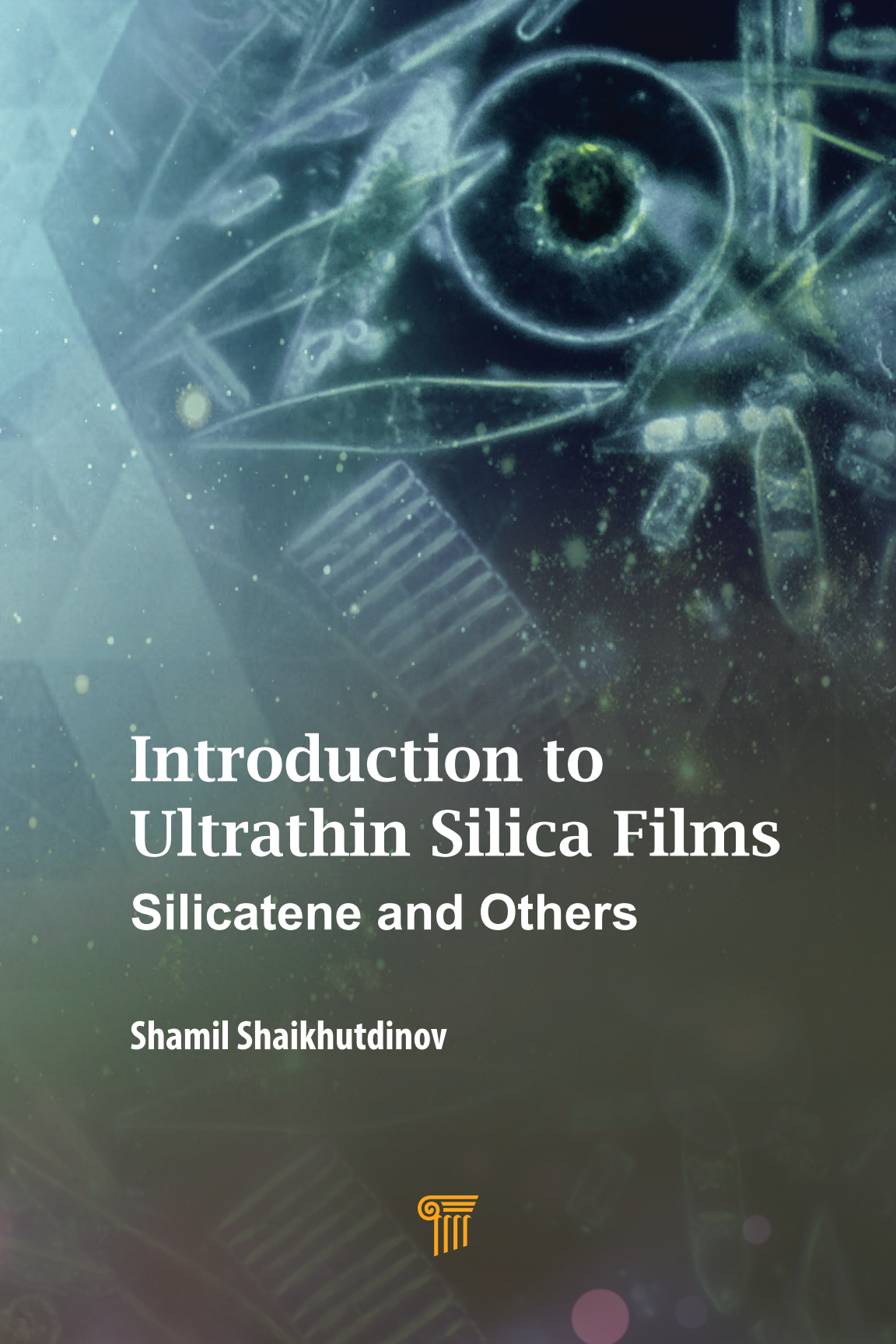

Introduction to Ultrathin Silica Films

Silicatene and Others

Shamil Shaikhutdinov

Introduction to Ultrathin Silica Films

Introduction to Ultrathin Silica Films
Silicatene and Others

Shamil Shaikhutdinov

JENNY STANFORD
PUBLISHING

Published by

Jenny Stanford Publishing Pte. Ltd.
101 Thomson Road
#06-01, United Square
Singapore 307591

Email: editorial@jennystanford.com
Web: www.jennystanford.com

British Library Cataloguing-in-Publication Data
A catalogue record for this book is available from the British Library.

Introduction to Ultrathin Silica Films: Silicatene and Others

ISBN 978-981-4877-28-2 (Hardcover)
ISBN 978-1-003-08862-2 (eBook)

To my parents,

to my family,

to my friends.

Contents

Preface

The idea to write this book came to me after I submitted a review paper for *Advanced Materials* entitled "Ultra-thin silica films on metals: The long and winding road to understanding the atomic structure," which summarized up-to-date information about preparation and structure of thin silica films on metal substrates, including historical excursion into how the atomic structure of what I later took the liberty to name "silicatene" was established. For those who are working like me in the fields related to catalysis, it is not surprising that early works on this topic were primarily driven by attempts to understand surface chemistry of silica and related materials widely used in heterogeneous catalysis. Obviously, chemical reactions on a solid-state catalyst occur on its surface, which is compositionally and structurally very complex in catalysts. It was reasonably thought that making use of many powerful techniques developed in surface science would help to elucidate the atomic structures and the mechanisms of chemical reactions on such catalytic materials if applied to less complex and better defined planar model systems. Since the early days of this so-called "surface science" approach to catalysis, it has been a goal to circumvent the well-known problems related to poorly conducting materials (most of catalytically relevant oxides are insulators or wide-band gap semiconductors) via preparation of well-ordered thin oxide films on metal substrates. Another practical advantage is that such samples can easily be cooled down or heated up, to monitor temperature effects. In addition, the reactions do not suffer from diffusion limitations, typical for porous materials, often obscuring intrinsic reaction properties. On the other hand, the metal support underneath a film may alter the surface composition of the oxide under study, and even stabilize structures which would

be unstable if unsupported. All these issues become of particular importance for *ultrathin* films. Although there is no firm definition of "how thick is ultrathin," I use this term for the films of a thickness below which physical and chemical properties deviate from those known for bulk samples and "thick" films. The thickness threshold depends on the material, but usually falls in the sub-nanometer range, which is comparable with the lattice parameters of an oxide. The recent progress in studies of ultrathin oxide films, in particular of transition metals, opened up a new playground for rational design of new-generation heterogeneous catalysts based on the thin-film technology.

While the chemistry-oriented studies of silica within the surface science approach (not only for catalysis, but with respect to dissolution, weathering, etc.) require preparation of relatively thick films hence representing bulk silica, the "materials science"-related disciplines and applications have a long-standing interest in the fabrication of ultrathin crystalline films for further miniaturization of metal-oxide-semiconductor transistors commonly using silica as the gate dielectric. In order to study fundamental properties of such materials, the preparation of *well-defined ultrathin silica* films is a necessity. Moreover, reducing the film thickness, one ultimately ends up with single-layer ("monolayer") films having a two-dimensional (2D) character by definition.

It is needless to say that single-layer materials have recently received enormous attention. The most famous one—graphene—triggered numerous investigations and search for other 2D materials. Silicon and germanium single layers, originally predicted on theoretical grounds, received experimental evidence, in fact, through their successful preparations on metal substrates and named "silicene" and "germanene," respectively. The studies were extended to tin and (very recently) iron layers called "stanene" and "ironene," respectively. Experimental studies carried out in our own laboratories in fruitful collaboration with prominent theoreticians allowed us to establish the atomic structure of the thinnest silica film that only consists of a single layer of corner-sharing SiO_4 tetrahedra. From a purely structural point of view, such a film can be considered as graphene composed of SiO_4 entities instead of the C atoms. Therefore, a single silicate layer deserves its place

in the continuously growing family of the truly two-dimensional materials and can be named "silicatene" in analogy to other analogs of graphene, although the suffix "-ene" for these materials may be confusing.

Certainly, those readers who address the structure and properties of silica for the first time, despite it being one of the most abundant chemical compounds on our planet, immediately recognize how much is known about this material and how important silica is in our daily life. Of course, there exist many comprehensive reviews and books about silica related to geoscience, catalysis, and materials science. However, I found reasonable to provide here some basic information about silica compounds, in particular their surface structures, which will be helpful for a better understanding of atomic structure of silica films and interfaces. Note also that the silicate layer constitutes a structural motif in layered (or sheet) silicates existing in abundance in the nature. I found also instructive to introduce the readers to the general considerations applied to the thin film growth, in addition to the basics of experimental tools commonly used in surface science studies of thin films. Dealing with thin silica films, one cannot avoid mentioning the "native" silica films formed by thermal oxidation of Si and SiC substrates. Such information is useful to judge the pros and cons of ultrathin films fabricated on metals, which is the core of this book.

To the best of my knowledge, there are no books on this topic to compare with, and hence to choose one or another scientific issue to highlight. Some sections are written in a free way as for oral lectures, and some text looks more like a scientific manuscript, although I tried to balance. My ultimate goal was to ease newcomers to join this, in my view, fascinating and rapidly growing up but still underrated field of metal-supported ultrathin films of silica and related materials.

I am very grateful to all my colleagues, with whom I worked for many years in the Department of Chemical Physics at the Fritz-Haber Institute of the Max Planck Society, for their tremendous work in the laboratories, in particular to Anibal Boscoboinik, Emre Emmez, Sarp Kaya, Linfei Li, Daniel Löffler, Junling Lu, Qiushi Pan, Dario Stacchiola, Héloïse Tissot, John Uhlrich, Xin Yu, Bing Yang,

and Jonas Weissenrieder. I want to thank Hajo Freund, who gave me the opportunity to head the group "Structure and Reactivity," who initiated the project and who was always in the heart of numerous debates and discussions. I was fortunate to collaborate with a great team of theoreticians, especially with Marek Sierka, Tanya Todorova, Radosław Włodarczyk, Itziar Goikoetxea, Frank Fischer, and Joachim Sauer (Humboldt Universität zu Berlin) and Philomena Schlexer, Gianfranco Pacchioni (Università degli Studi di Milano-Bicocca). Without their contribution, this work could never have been completed.

Finally, I want to thank my family, who supported me in this from the first day and provided me the best conditions for writing this book. This support is invaluable.

Shamil Shaikhutdinov
Berlin, January 2020

$^{16}O^{18}O$.[3] Therefore, oxygen in the silicate film does not exchange with oxygen in the gas phase, and the Ru surface interacts solely with the ambient O_2 molecules penetrating the film. Direct comparison of the silica-covered and silica-free surfaces shows, however, that surface reactions on metals, in this case oxidation, may proceed very differently in confined space formed by a weakly bound silicate.

Even stronger passivation effect is observed for the aluminosilicate bilayer films. One possible explanation could be a smaller distance between the film and the Ru surface as compared to pure silicate that would, in turn, suppress oxygen intercalation. Another factor that might influence the reaction is that charge imbalance caused by Al^{3+} substitution of Si^{4+} in the framework is likely compensated via the charge transfer from the metal support. The additional electrostatic forces between the Al-silicate and the metal surface could also affect the reaction.

To conclude, bilayer silicate films is very stable in the oxidizing atmosphere and effectively passivate the metal surface. The results also indicate a considerable confinement effect on the metal oxidation.

7.1.2 Hydrogen

Since the silicate films are terminated by fully saturated siloxane bonds, hydrogen adsorption shows essentially no effect on surface structures. In particular, no hydroxyls are formed even by exposure to 10 mbar of hydrogen, which is in the "surface science" community considered as a "high pressure." In fact, all changes observed upon H_2 exposure only relate to adsorption on the metal substrate.

In order to study interaction of hydrogen with bilayer films in details, in particular to see whether hydrogen intercalates the interface like oxygen discussed above, one first needs to get rid of O ad-atoms, which are always present in some amounts in the "as prepared" films. In principle, they can desorb, at least partially, upon vacuum annealing that usually requires high temperatures depending on the metal support. In fact, a more efficient way to remove O from metal surfaces at mild conditions is to expose it to hydrogen or carbon monoxide (CO) which react with O to form water (respectively, CO_2), desorbing at much lower temperatures

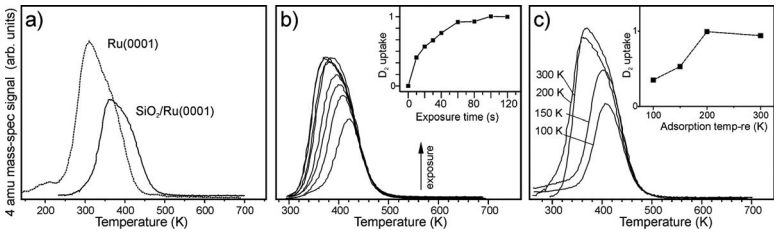

Figure 7.2 (a) TPD spectra of D_2 at saturation coverage measured on the bare Ru(0001) surface and on SiO_2/Ru(0001) film. (b,c) TPD spectra measured on SiO_2/Ru(0001) after exposure to 10^{-6} mbar of D_2 as a function of exposure time all at 300 K (b), and of adsorption temperature all at 2 min exposure time (c). Integral intensities (D_2 uptakes) are shown in the insets. Adapted with permission from ref. 5.

than O_2. Interestingly, exposure of bilayer films to hydrogen at the UHV-compatible pressures (typically, 10^{-6} mbar) showed no effect. Either H_2 molecules cannot penetrate the silicate and hence reach the metal surface at these pressures or, most likely, the O ad-atoms block H_2 dissociation necessary for its reaction with O. Only at elevated pressures (0.1–1 mbar) is it possible to get rid of O species from the interface and actually replace them by H ad-atoms, which, in turn, desorb as H_2 upon thermal flash leaving the metal surface clean.

For studying interaction of hydrogen with solids, it is common to use deuterium (D_2) which is better suited for TPD and IRAS measurements, but the conclusions hold true for hydrogen as well. Figure 7.2a compares two TPD spectra measured after prolonged exposure of bare Ru(0001) and SiO_2/Ru(0001) film surfaces to D_2 until saturation. Although the absolute intensities considerably differ, the desorption profiles are quite similar. In addition, desorption from the silica films looks like shifted to higher temperatures by ~30 K. In this respect, it is worth mentioning that O_2 desorption signal at around 1000 K coming from the decomposition of Ru-oxide underneath the film also showed a shift to higher temperatures (see Fig. 7.1a).

As expected, the amount of hydrogen intercalating the interface increases with exposure time as shown in Fig. 7.2b. The uptake at saturation is practically independent of the hydrogen pressure used,

i.e., 1 mbar vs. 10^{-6} mbar. The adsorption kinetics follows the one observed on bare Ru(0001). Therefore, all findings point out that hydrogen can easily intercalate the interface as if the silicate layer is transparent for the H_2 molecules. However, adsorption experiments at low temperatures showed that the hydrogen uptake considerably, by a factor of 2, *decreases* (Fig. 7.2c), whereas on the clean Ru(0001) surface the uptake *increases*. Apparently, the permeation of $H_2(D_2)$ molecules through the silicate film depends on temperature. On the other hand, one cannot exclude the possibility that the $H_2(D_2)$ dissociation and diffusion of H(D) atoms on the Ru surface is affected by silicate layer above, thus manifesting the confinement effects.

The results shown above are obtained for the Ru-supported films. Similar experiments were also carried out for Pd-supported films (see Section 7.1.4 below).

7.1.3 Carbon Monoxide

It becomes clear now that one should take into account gas permeation through the film in order to rationalize the environmental effects on metal-supported silicate bilayer films. Since the siloxane terminated surface is inert, a bilayer silicate film behaves, in essence, as a membrane or a molecular sieve having a certain pore size distribution. The film reaction to the ambient gases is primarily determined by adsorption and reactions on the metal support which, in turn, may be affected by the silicate layer. In case of hydrogen, it is quite difficult to detect and differentiate H adspecies by conventional electron and vibrational spectroscopies. In this respect, CO is a molecule that is better suited for studying permeability of our films by making use of the metal surface as a CO "detector." Of course, the metal surface must first be cleaned from any adsorbates formed during the film preparation, either by UHV annealing or by reaction with hydrogen as discussed above.

To monitor CO adsorption kinetics, IRAS spectra were continuously recorded immediately after introducing CO into the vacuum chamber. Since the intensity of an IRAS band not always correlates with the surface species population for several reasons, it is recommended to complement the IRAS results with TPD

measurements which allow to determine total amount of CO on the sample surface. The IRAS and TPD experiments were performed at different adsorption temperatures and pressures, as illustrated in Figs. 7.3 and 7.4 for Ru(0001)-supported films. The results on SiO_2/Pd(111) will be presented in the next section for comparison.

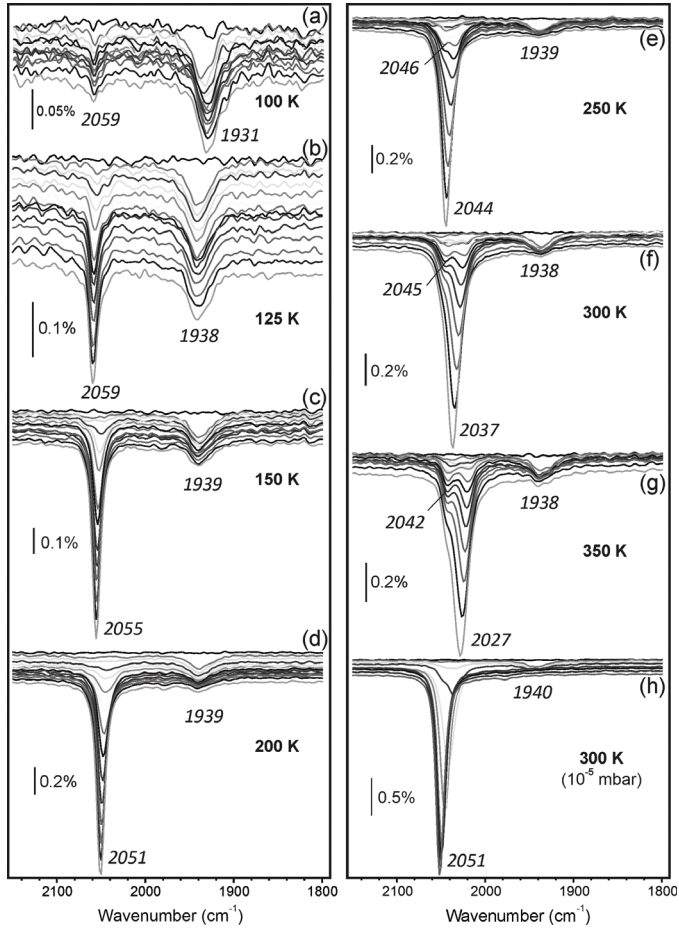

Figure 7.3 Consecutively recorded IRAS spectra (from top to bottom in every panel) on SiO_2/Ru(0001) exposed to 2×10^{-6} mbar CO (a–g) and 10^{-5} mbar CO (h) at the indicated temperatures. Each spectrum takes ca 12 sec. Spectra are offset for clarity. Reproduced with permission from ref. 5.

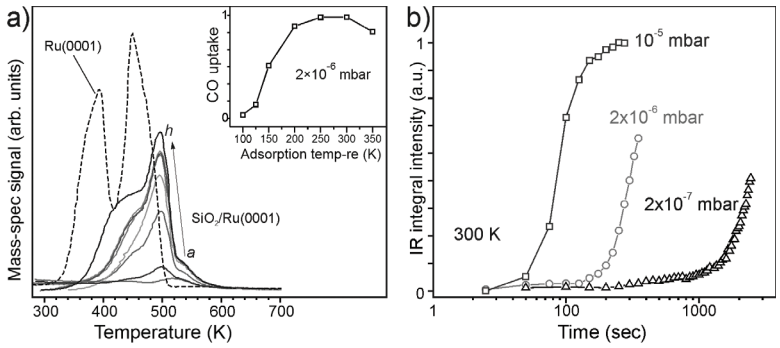

Figure 7.4 (a) TPD spectra of CO measured after taking the last IRAS spectra shown in Fig. 7.3(a–h). (The spectra are cut off at 300 K). The inset shows CO uptake as a function of adsorption temperature at constant pressure. CO TPD spectrum on the clean Ru(0001) surface at saturation is shown for comparison. (b) Kinetics of CO adsorption measured by IRAS at three different CO pressures as indicated. Note the logarithmic scale for the exposure time. Adapted with permission from ref. 5.

A weak band at around 1940 cm^{-1} appearing immediately at all temperatures most likely originates from CO adsorption on the silica uncovered spots and will be omitted in the following discussion. The spectra are dominated by the band(s) in the 2030–2060 cm^{-1} region depending on the exposure conditions. The band bears close similarity to CO adsorption on the clean Ru(0001) surface. In particular, it was established that the band position almost linearly correlates with CO coverage, i.e., the higher the coverage the higher the frequency.[6] At low temperatures, the signal at 2059 cm^{-1} is weak, although the frequency itself suggests the highest CO coverage. The band gains in intensity with increasing adsorption temperature, but shifts to the lower frequencies as if the CO coverage diminishes, which is at a variance to the TPD-measured CO uptake increasing (see inset in Fig. 7.4a). The discrepancy can be rationalized by that the band position reflects a *local* CO density rather than average CO coverage determined by TPD. In fact, the band only approaches the highest frequency at the highest CO coverage upon exposure to 10^{-5} mbar CO at 300 K as shown in Fig. 7.3h.

Basically, TPD spectra recorded after each IRAS experiment look similar to those obtained for bare Ru(0001) (Fig. 7.4a). However, desorption traces are shifted towards higher temperatures, by about 25 K if measured at the descending desorption edge. Without any knowledge of the system under study, one would assign such a shift to a stronger CO bonding. Recall, however, that such shifts were observed for O_2 and D_2 dissociative adsorption as well (see Figs. 7.1 and 7.2), and as such it becomes common for desorption processes from the intercalated silicate/metal interface. It appears more plausible that the observed shifts in TPD spectra originate from the time delay that is needed for a molecule to find the pore in the silicate film to escape into the vacuum.

Figure 7.4 shows that the CO uptake decreases at low temperatures and drops almost to zero at 100 K, in nice agreement with IRAS results. However, this is purely a kinetic effect. As depicted in Fig. 7.4b, CO adsorption exhibits the induction period. The time needed for the adsorption to set in inversely correlates with the pressure: The higher the pressure, the shorter the induction period. This finding can hardly be explained if CO penetrates the film uniformly through all *N*-membered silica rings. Apparently, only large size rings are suited for CO penetration.

CO adsorption on a metal-supported silicate bilayer film was further studied using density functional theory (DFT) calculations.[7] As the dispersion forces play a critical role in this system, various dispersion corrections at the DFT level have been examined for a crystalline film only. Figure 7.5(a,b) shows optimized geometries for CO adsorbing in different positions on Ru(0001) at the lowest coverage, i.e., 1/16 ML. As in the case of bare metal surface, CO prefers the on-top sites with the adsorption energy −2.3 eV, which is almost equal to that calculated for bare Ru(0001) (−2.26 eV) and much higher than for CO in the hcp site (−1.43 eV). Trapping CO in the silicate cage is thermodynamically unfavorable: The energy gain is small, only about 0.1 eV. At high coverages, the adsorption energy is considerably reduced (−1.84 eV), and the CO stretching frequency becomes comparable which that measured in the experiment. Note that, at this high coverage, the interface gap increases dramatically, from ∼260 to ∼590 pm, measured between the Ru and O layers for the CO-free and CO intercalated films, respectively. In addition, this

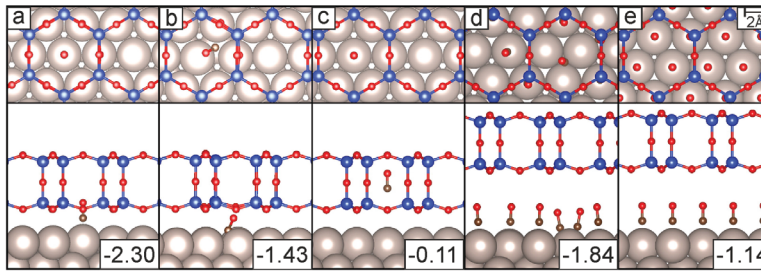

Figure 7.5 (a,b) Optimized geometry of CO at low coverage (1/16 ML) in top (a) and hcp (b) positions on Ru(0001). (c) CO inside the silica cage. (d,e) CO ad-layer at high coverages: 5/8 ML (d) and 1 ML (e). 1 ML (monolayer) corresponds to the surface density of Ru atoms. The calculated adsorption energies (in eV) are indicated. Reproduced with permission from ref. 7.

may explain the experimentally observed small ($\sim$5 cm^{-1}) blue-shift of a phonon band at 1300 cm^{-1} due to further decoupling of a film from a Ru substrate covered by CO. Finally, the authors estimated barrier for diffusion of CO through the unsupported crystalline silica bilayer ($\sim$0.5 eV) computed using a potential energy curve obtained from a constrained optimization, not a real barrier for diffusion.

7.1.4 SiO_2/Pd(111) vs. SiO_2/Ru(0001)

Adsorption experiments over bilayer silicate films prepared on Pd(111) revealed some similarities as well as differences if compared to the films grown on Ru(0001). Note that both CO and H_2 readily adsorb on Pd(111), and the adsorption mechanism is well documented in the literature that allows to identify adsorbed species by IRAS and/or TPD.

Figure 7.6a presents a series of IRAS spectra continuously recorded at room temperature in CO at pressures increasing from 1×10^{-7} to 5×10^{-6} mbar. At low exposures (*ca.* 10 Langmuir (*L*), 1 $L = 10^{-6}$ Torr$\times$sec), no CO adsorption is found, suggesting that the film fully covers the metal surface. At increasing CO dosage, a broad feature develops at 1930 cm^{-1}, which gains in intensity and shifts to 1935 cm^{-1}. In order to accelerate CO uptake, the pressure was increased to 10^{-6} mbar. At 200 L of CO, an additional band

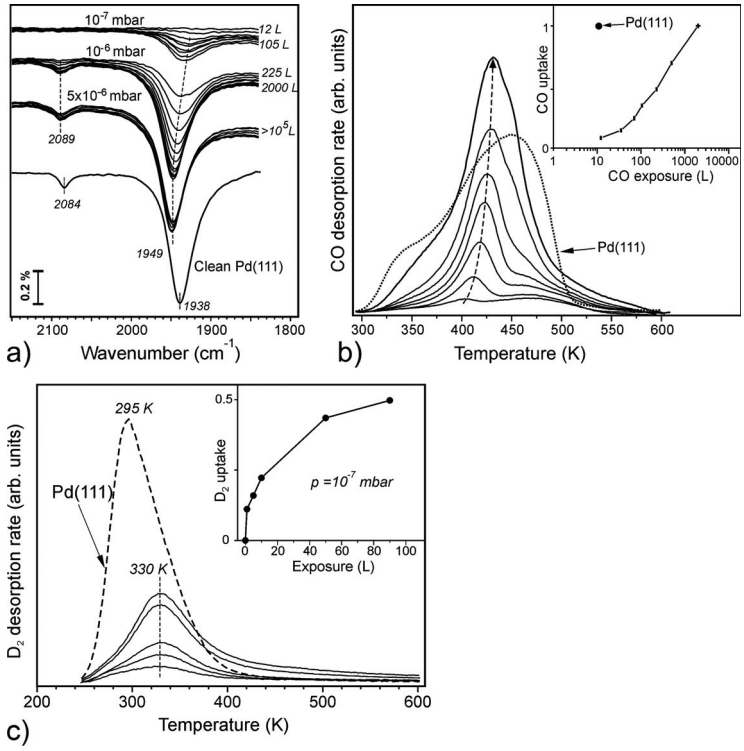

Figure 7.6 (a) Consecutive IRAS spectra measured at 300 K on a SiO_2/Pd(111) film at CO pressures as indicated. The spectra are offset for clarity. The total CO exposures (in L) are shown adjacent to the spectra. The spectrum for the clean Pd(111) surface exposed to 10 L is also shown for comparison. (b) TPD spectra at increasing CO dosage at 300 K. The spectrum for bare Pd(111) at 10 L is shown for comparison. Inset shows CO uptake as a function of CO exposure (in the logarithmic scale). (c) TPD spectra of D_2 on SiO_2/Pd(111) as a function of exposure at 250 K. The inset shows D_2 uptake normalized to the one on bare Pd(111) obtained after dosing 1 L onto clean Pd(111), also shown for comparison. Adapted with permission from ref. 8.

appears at 2089 cm^{-1}. The bands grow and saturate at very high exposures (10^4 L) reached by increasing CO pressure. At saturation, a strong band at 1949 cm^{-1} and a weak signal at 2089 cm^{-1} are observed. The peak positions and the intensities are almost identical to those (1938 and 2084 cm^{-1}) obtained on saturation of the clean Pd(111) surface even at the lowest CO exposure studied.

The bands are associated with CO adsorbed in bridge and top sites, respectively. Therefore, we can conclude that CO readily intercalates the interface between the silicate and the Pd surface. The conclusion is fully supported by TPD results shown in Fig. 7.6b. The CO uptake at saturation is almost equal to that measured on bare Pd(111). However, the process is rather slow at room temperature as it needs relatively high exposures, again suggesting that CO penetrates most likely through the largest silica pores. Similarly to Ru-supported films, the uptake vs. exposure curve exhibits the induction period on Pd(111) supported films as well.

TPD spectra of CO on Pd(111) are well understood.[9] On heating of the saturated CO adsorbed layer, CO molecules first desorb from the most weakly bound, on-top sites followed by desorption from the bridge sites (at $T < 400$ K). The remaining CO molecules diffuse and occupy the threefold hollow sites, from which they desorb as a peak at 450 K (see the spectrum in Fig. 7.6b). At initially very low coverage, CO only occupies the hollow sites, and the desorption peak shifts to lower temperatures at increasing coverage (up to 1/3 ML) due to repulsive CO–CO interaction.

Although CO desorbs from SiO_2/Pd(111) in the same temperature range, the desorption profiles showed certain difference to bare Pd(111) (Fig. 7.6b). In addition, the most prominent desorption peak at around 400 K shifts to *higher* temperatures at increasing CO dosage, whereas the desorption maximum on pure Pd(111) shifts to *lower* temperatures.[9] The observed peak shift may, again, be associated with the time needed for the CO molecules underneath the film to find an appropriate pore to escape.

As far as adsorption of hydrogen is concerned, Fig. 7.6c collects TPD spectra of D_2 at increasing exposure. In principle, hydrogen desorbs in the same temperature range as for the clean Pd(111) surface, but there are some differences between two systems. In contrast to Pd(111), D_2 desorbs from SiO_2/Pd(111) at high temperature (330 K) independently of the coverage, whereas the maximum peak on Pd(111) gradually shifts to the lower temperatures at increasing dosage.[10] The D_2 uptake increases non-linearly and approach saturation which is remarkably, by a factor of 2, smaller than on bare Pd(111).

On the Ru(0001)-supported films, the D_2 uptake correlates well with the CO uptake. However, on the Pd(111) supported films the D_2 uptake is substantially lower than the CO uptake. (In both cases, the comparative CO and D_2 measurements were performed using the same sample in order to minimize any instrumental effects.) It is tempting to link the difference between Pd and Ru to the well-known specific H_2/Pd interaction resulting in almost spontaneous migration of H(D) atoms into the Pd bulk and formation of Pd hydrides, which does not occur on Ru. Apparently, some D adatoms diffusing underneath the silicate film migrate into the Pd bulk on heating and hence become unavailable for desorption into the vacuum, thus reducing the total amount of D_2 measured by TPD. If so, then this finding provides one more example of confinement effects.

DFT calculations of CO adsorption on silica covered Pd(111) revealed rather small effects on adsorption energies.[8] The hollow sites on Pd(111) are most favorable for both systems, although the adsorption energy per CO molecule decreases with increasing coverage (Table 7.1), i.e., from −2.17 eV (0.25 ML), to −1.87 eV (0.5 ML), and to −1.59 eV (0.75 ML). The adsorption energies for CO underneath the silica follow the same trend and are −1.91, −1.73, and −1.51 eV, respectively. Accordingly, the differences in adsorption energies between clean and silica covered Pd(111) become smaller at high coverages. As in the case of Ru(0001) supported films, intercalation of CO causes the interface distance to remarkably increase, from 3 to 6 Å. Although performed solely on crystalline silica overlayer the calculations showed fairly good agreement with experimental results.

Table 7.1 Adsorption energy E_{ads} (in eV) per CO molecule adsorbed in threefold hollow sites on Pd(111) and SiO_2/Pd(111)

Coverage (ML)	**1/4**	**1/2**	**3/4**
Pd(111)	−2.17	−1.87	−1.59
SiO_2/Pd(111)	−1.91	−1.73	−1.51
ΔE_{ads}	0.26	0.14	0.08

Source: Taken from ref. 8.

7.1.5 General Mechanism

We may now speculate about what happens when a bilayer silicate film is exposed to "simple" gases like oxygen, hydrogen, and carbon monoxide. Obviously, the silicate layer itself is inert towards such gases. However, gas molecules penetrate through the film and react with the metal surface underneath. Let us first consider the case of CO for which the experimental and theoretical database is the most complete. We neglect macroscopic "holes" exposing bare metal surface in the discontinuous films since CO immediately adsorbs there and the related spectral features remain unchanged during the experiment.

We first assume that CO penetrates the silica film without any barrier. CO adsorbs on the metal surface sites right behind the pore and then can either desorb back through the same pore or diffuse across the metal surface underneath the silicate. CO diffusion even on the bare metal surfaces is not trivial issue. First, the diffusion coefficient is difficult to measure, and, second, it often depends not only on temperature, but also on coverage due to the lateral CO–CO interaction. Nevertheless, the estimated diffusion length for the time-scale of our IRAS experiments ($>$10 sec) is relatively large, about 10^3–10^4 nm at room temperature, but becomes comparable with the interatomic distances at cryogenic temperatures. Certainly, diffusion underneath the film is, at least, not as fast as on bare surface. Therefore, upon exposure at low temperatures, first adsorbed CO molecules hardly diffuse across the surface, and the next incoming CO molecules cannot penetrate through the same pore as the adsorption site is already occupied. Therefore, very small CO uptake measured at low temperatures probes solely the largest silica rings present either at line defects or in amorphous portions of the film (see Chapter 5). The low diffusivity of CO, in turn, results in high local concentration of adsorbed CO molecules near the pore they entered. Indeed, the 2059 cm^{-1} band observed at low temperatures on Ru-supported films (see Fig. 7.3) suggests CO coverage of about 0.5 ML, whereas the total coverage measured by TPD is an order of magnitude lower. In addition, this finding suggests that CO does not penetrate every silica ring, but only the largest ones. Based on the kinetic diameter

of CO (~3.8 Å), there are must be relatively large silica rings for molecules to go through. Note that in the adsorption experiments, gas phase molecules possess the kinetic energy corresponding to the room temperature. Therefore, the low temperature effect on CO uptake, shown in Fig. 7.4a, cannot be explained in terms of ballistic flow through the pores. Most likely, the temperature effect reflects the activated process.

The induction period and the following-up self-acceleration of the CO adsorption demonstrated by Figs. 7.4b and 7.6b are intriguing. In principle, such a behavior is indicative of non-linear processes. For instance, CO surface diffusivity on metals considerably enhances at increasing coverage due to the CO–CO repulsive interaction. In our case, the increased local CO coverage right behind the pore may lead to the situation when CO diffusion rapidly increases above the critical coverage. Another explanation is based on the theoretical prediction, yet unproven experimentally, that intercalated CO at high coverages pushes the silicate layer away from the metal surface (Fig. 7.5). Accordingly, CO diffusion underneath the silica layer will be certainly enhanced once this locally happened. Such "gate lifting" model has to be further examined, for example, by scanning tunneling microscopy (STM), particularly at various temperatures.

Certainly, the adsorption kinetics is more involved in case of dissociating molecules like hydrogen and oxygen. Despite the limited database of experimental results, the H(D) atoms on the bare metal surfaces are theoretically predicted to diffuse very fast at our temperatures studied. Therefore, they can migrate far away from the place they penetrated through the film and dissociated, thus resulting in their fairly uniform distribution on the metal surface. On heating during the TPD run, the H ad-atoms desorb as H_2 via recombinative mechanism. As the desorption temperature and time are directly linked in TPD through the heating rate (β), $T = T_0 + \beta \times \text{time}$, any time delay immediately causes the desorption profile shifting to the higher temperatures. For the heating rate 3 K/s applied in the above-shown TPD experiments, the obtained shift of ~30 K (see Fig. 7.2a) corresponds to about 10 sec of delay for CO desorption from the silicate covered surface. In other words, ad-species spend about 10 sec, on average, to find the right pore

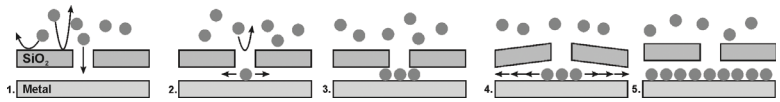

Figure 7.7 General scenario of gas adsorption on bilayer silicate films.

to escape into the vacuum, which is enormously long for the flat surfaces! Therefore, the H ad-atoms on the silicate-covered Pd(111) surface have enough time to migrate into the Pd bulk rather than to desorb into vacuum through the film, resulting in a lower hydrogen uptake measured by TPD. The hydride formation is well-known phenomenon for Pd, and not for Ru, that may explain the difference between the two systems.

A general scenario of what may happen to the metal-supported bilayer silicate films exposed to ambient gases is schematically shown in Fig. 7.7. For simplicity, it only considers non-dissociative adsorption on a metal substrate. (1) A molecule penetrates through the large pores present in the amorphous portions of the film and line defects most likely via an activated process. The crystalline layer is either impermeable or exhibits large activation barrier. (2) The molecule adsorbs on the metal surface right behind the pore. Next molecules only penetrate through the same pore if the ad-molecule makes the site free by hoping into adjacent site if available. At low temperatures, the process ends with (3). The metal surface around the pore exhibits a high local density of adsorbed species, whereas the total coverage is low. If, however, the diffusion across the surface becomes possible (e.g., at increasing temperature), then such area expands. Concomitantly, the silicate layer lifts up (4), thus making the surface diffusion facile and accelerating the adsorption until it reaches saturation (5). Apparently, a critical coverage and/or area size exists, which must be formed during the induction period, before the accelerated migration takes place through the "open gate."

7.2 Bilayer Film as the Thinnest Silica Membrane

In previous sections, we discussed primarily experimental results showing that ambient gas molecules migrate through a silicate film

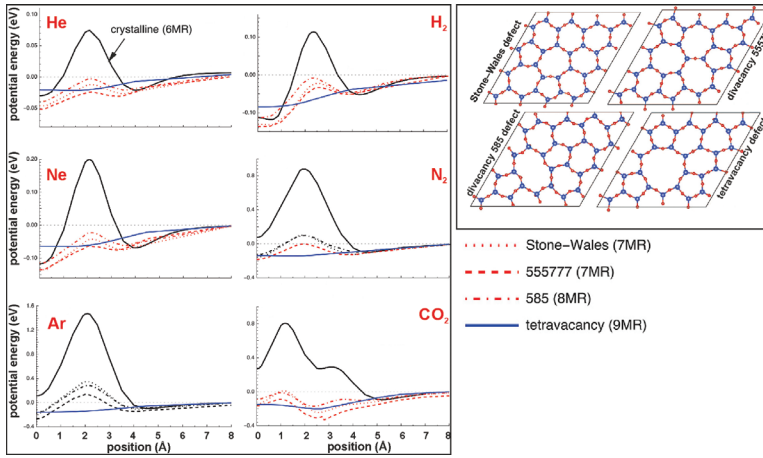

Figure 7.8 On the right: Top views of silica bilayer geometries used to mimic different *N*-membered rings. On the left: Potential energy profiles for different gases as a function of position, measured from the mirror plane in the bilayer to the center of the molecule. Only the unique portion of the symmetric potential energy is plotted. The curves are labeled for all plots. Adapted with permission from ref. 11.

like a membrane. In fact, bilayer silicate constitutes the thinnest possible stable structure for a silica membrane. If one includes the van der Waals radii of the surface oxygen atoms (1.52 Å), it is only 7.2 Å in thickness. Although its practical realization in the membrane technologies is hardly possible in the very near future, we address here some fundamental aspects related to the gas permeation through such nanoporous membranes. For this, we refer to the DFT calculations[11] for free-standing silica bilayers of different geometries comprising crystalline (i.e., of six-membered rings) as well as the seven-, eight-, and nine-membered rings. The models are depicted in Fig. 7.8 also showing the potential energy profiles computed at the DFT + D (dispersive corrections) level for gas passage through these various pore types for several molecules.

Basically, three different types of potential energy profiles are found, depending on the relative sizes of the gas and silica ring. Consider the example of He. It shows a minimum on the silica

surface corresponding to a physisorbed molecule about 4 Å from the center, a maximum as it enters the silica ring (at ~2 Å), and another minimum (at 0 Å) exactly between the silicate layers, thus corresponding to a trapped molecule inside bilayer. This Type I is observed when the size of the gas molecule is larger than or comparable to the size of the pore. For He and Ne, this occurs only for passage through the crystalline layer. For the larger Ar atom, this type of repulsive barrier also occurs for all of the seven- and eight-membered rings.

Like the Type I, the Type II consists of two local minima (one on the exterior surface and one inside the bilayer) and a local maximum. The difference is that the local maximum has an attractive (negative) potential energy as compared to the non-interacting gas–silica system (see, for example, dashed lines for He and Ne). Thus, the Type II has no barrier for ballistic gas transport (because the entering gas molecule will have a positive kinetic energy), but does have an effective barrier for gases attempting to enter the pore after being physisorbed on the surface. This occurs when the pore is slightly larger than the gas molecule, e.g., for He and Ne with all of the seven- and eight-membered ring defects, but never for Ar or larger molecules. Both Type I and Type II profiles have stable states for the gas molecule within the bilayer. For He and Ne, this interior trapped states are thermodynamically more stable than the physisorbed surface state. For Ar transport through the crystalline six-membered ring, this interior state may be kinetically trapped by the large potential energy barrier for exit, despite being significantly higher in energy than the free gas. This interior state is increasingly stabilized for the various seven- and eight-membered rings, due to the surrounding attractive dispersion interactions.

Finally, Type III profiles have no barrier, and consist of approximately only a single local energy minimum within the bilayer. This type occurs when the gas molecule is significantly smaller than the pore. Nine-membered ring structures arising from the tetravacancy defect have no energy barrier for any of the gases considered here, and may therefore serve as the most possible candidate for the pores responsible for gas penetration in the metal-supported films discussed in the previous sections.

The energy profiles of H_2 are qualitatively similar to that of the comparably sized He atom. The N_2 profiles are qualitatively similar to that of Ar. The larger triatomic CO_2 molecule has additional features. First, CO_2 has a lower potential energy barrier for entry than N_2 for all of the defects. If one considers both molecules as cylinders, CO_2 has a smaller effective diameter than N_2, due to the electron density distribution. The lower potential energy barrier for entry of CO_2 is especially pronounced for the seven- and eight-membered rings. Second, the potential energy surface has an additional local minimum and local maximum, as the C and O atoms in the CO_2 molecule interact with distinct layers of the silica structure. Finally, for the nine-membered ring, the minima occur at 2.5 Å, and are separated by 0.05 eV at the geometric center of the bilayer. This is qualitatively similar to the Type III for N_2, but with a larger central barrier.

The DFT results provide a basis for calculating relative permeances, which in turn allow to estimate the selectivity of the different pore structures for the different molecules in gas mixtures. In general, the transmission process consists of several intermediates and transition states, which can be used to compute the barrier crossing rates by applying classical transition state theory. However, in a crude approximation, these multistep processes can be described in terms of the energetic span, δE, which is the largest energy difference between an intermediate (local minimum) and any subsequent transition state (local maximum) during the barrier crossing process. The energetic span serves as apparent activation energy of the process, and thus a smaller energetic span leads to a faster reaction. Table 7.2 shows the computed energetic span values for the gases transiting through the various silica bilayer.

The selectivity for two gases, X and Y, is the ratio of the transport rates, r_X and r_Y, respectively, each of which in turn can be expressed in terms of the classical Arrhenius rate equation $S_{X/Y} = \frac{r_X}{r_Y} = \frac{A_X e^{-\delta E_X / k_B T}}{A_Y e^{-\delta E_Y / k_B T}}$. For simplicity, one can assume pre-exponential factor to be equal for both molecules. In (more realistic) case of amorphous silicate film having a certain ring size distribution, the selectivity can be obtained by weighting the selectivities by the transmission of each ring type by the probabilities (p_i) at

Table 7.2 Energetic span, δE (in eV), for several gases transiting through bilayer silica

Structure	He	Ne	H_2	CO_2	Ar	N_2	CO	Kr
Crystalline (6)	0.104	0.316	0.232	0.900	1.576	0.977	0.962	2.554
Stone–Thrower-Wales	0.046	0.136	0.132	0.254	0.520	0.259	0.259	0.882
555777	0.051	0.136	0.137	0.330	0.406	0.184	0.211	0.710
585	0.039	0.114	0.113	0.170	0.444	0.224	0.205	0.572
Tetravacancy	0.022	0.065	0.085	0.202	0.160	0.143	0.142	0.245

Note: The corresponding structures are shown in Fig. 7.8 (from ref. 11).

which each ring type is observed: $S_{X/Y} = \frac{\sum_i p_i e^{-\delta E_{X,i}/k_B T}}{\sum_j p_j e^{-\delta E_{Y,j}/k_B T}}$. The calculations using the energy span (δE) values, presented in Table 7.2, and experimentally observed ring size distribution in Chapter 5 showed that the crystalline film has sufficiently high permeances and selectivities, which allows to consider it even for practical applications in industrially important H_2/CO and He/CH_4 separations. Not surprisingly, the amorphous silicate increases the permeabilities of all gases due to the smaller potential energy barriers for the larger rings. As a result, transport through the larger rings dominates, but the selectivity falls off.

It is interesting that DFT results suggest a non-zero probability for small molecules to be trapped inside the silica bilayer, either thermodynamically, i.e., showing the lowest energy in potential energy profiles, or kinetically, due to the large barrier to exit. This would allow to use certain inert gases as selective probes for particular ring size to measure the ring size distribution in entire films, which was thus far investigated only locally using microscopy techniques like TEM and STM. Moreover, such systems would be interesting for atomistic studies of gas absorption on nanoporous materials like zeolites. To date, our own attempts to experimentally detect trapped molecules by TPD were unsuccessful. However, a recent study[12] demonstrated that Ar might, indeed, be trapped in bilayer films during XPS measurements in Ar atmosphere. Tentatively, the effect has been assigned to the ionization of Ar atoms by X-rays.

7.3 Chemical Reactions under Bilayer Silica Films

The results presented in previous sections clearly demonstrate that environmental effects on structure and properties of metal-supported bilayer silicate films primarily involve adsorption and reaction on a metal substrate underneath. The system can be viewed as a nanoporous silica membrane coating the metal surface, on which chemical reactions take place in space limited in one direction to a few Angstroms. In addition to that the silicate film controls both the access of reactants and the removal of products and hence the reaction equilibrium according to Chatelier's principle, the spatial confinement can also alter the reaction kinetics through the modification of the transition state and/or by changing the reaction pathway. Therefore, surface chemistry in these kind of materials becomes more complicated. On the other hand, it may result in new functional properties anticipated for such hybrid systems.

To illustrate the complexity of processes occurring on silicate covered metal surfaces, we address a reaction of oxygen removal from the SiO_2/Ru(0001) interface by hydrogen. In the experiments described below, the "O-rich" film containing O ad-atoms at the interface was exposed to 10^{-6} mbar of H_2 at elevated temperatures (540–650 K). Based on XPS results, all O atoms are ultimately removed from the interface upon this treatment. Obviously, hydrogen diffuses to the interface, dissociates there to produce atomic H which react with O to form water that desorbs. Since water was not detected (neither by XPS nor by IRAS) during the reaction, it probably desorbs through the silicate layer immediately upon formation.

The process was visualized in situ by low-energy electron microscopy (LEEM).[13] LEEM movies during sample heating monitor the reaction via a change in image intensity (local darkening). Figure 7.9 displays a series of snapshots showing the reaction propagating from the bottom right to the upper left. Combined LEEM and XPS results of bright and dark regions identify the support underneath as "O-rich" and clean Ru(0001) surfaces, respectively. Although the reaction front showed no preferential directions, step bunches (highlighted by arrows in the images) seem to hamper its propagation.

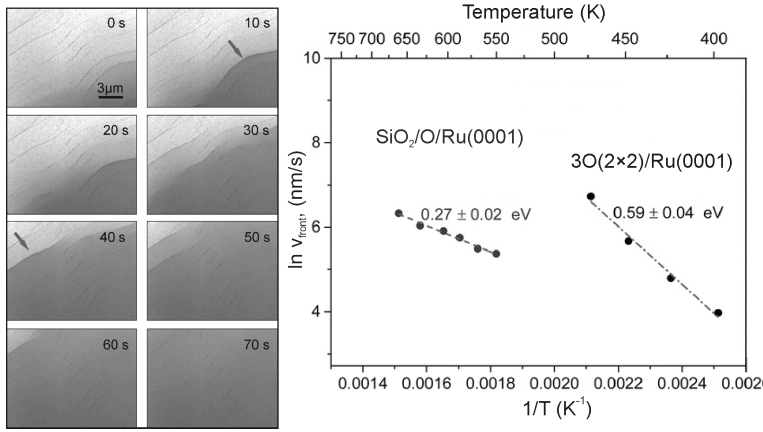

Figure 7.9 On the left: Snapshots from the LEEM movie of the reaction propagating across the "O-rich" SiO_2/Ru(0001) surface in 10^{-6} mbar H_2 at 550 K. The arrows highlights step bunches decelerating the reaction front. On the right: Arrhenius plots of the front velocities on "O-rich" SiO_2/Ru(0001) and 3O(2×2)/Ru(0001). Adapted with permission from ref. 13.

The same set of experiments performed on the silica-free 3O(2×2)-Ru(0001) surface also revealed the reaction front propagation which sets in at a much lower temperatures (400–500 K) and therefore proceeds too fast to be precisely measured at the temperatures used for the silica samples. This is not surprising, since hydrogen can freely access the Ru surface and also water desorbs easier. The temperature dependence of the front velocity showed the Arrhenius behavior, from which the apparent activation energy (E_{act}) was determined, i.e., 0.59 ± 0.04 eV, in good agreement with previously reported values determined from TPD measurements. The H_2 + O/Ru(0001) reaction is commonly described in several elementary steps:

$$H_{2(gas)} \rightleftharpoons 2H_{(ads)} \tag{7.1}$$

$$H_{(ads)} + O_{(ads)} \rightleftharpoons OH_{(ads)} \tag{7.2}$$

$$OH_{(ads)} + H_{(ads)} \rightleftharpoons H_2O_{(ads)} \tag{7.3}$$

$$2OH_{(ads)} \rightleftharpoons H_2O_{(ads)} + O_{(ads)} \tag{7.4}$$

$$H_2O_{(ads)} \rightleftharpoons H_2O_{(gas)} \tag{7.5}$$

As the first step includes H_2 dissociation, the reaction can only proceed within the "dilute" O ad-layer having empty sites for dissociate. Apparently, the reaction starts at some structural defects or where local fluctuations allow H_2 dissociation to occur. The associative reaction (7.2) is believed to be the rate determining step.

The temperature dependence on reaction over silicate covered surface showed the Arrhenius behavior with $E_{act} = 0.27 \pm 0.02$ eV, which is almost two times smaller than on the bare Ru surface. In addition, the pre-exponential factor is substantially smaller, by a factor of 10^4. The origin of the difference between the activation energies remains not fully understood. As discussed in previous sections, H_2 readily penetrates through defects in bilayer film, thus leaving the step (7.1) unaltered or only slightly affected by the silica layer. In contrast, water desorption (7.5) that occurs spontaneously on uncovered Ru is most likely hampered by silica overlayer. Theoretical considerations of water diffusion in silica, performed on small silica cluster models, suggested about 1.5 eV for the activation barrier for the six-membered ring, but decreases down to 0.3 eV for the seven-membered cage.[14] Since water formed by reactions (7.3) and (7.4) has to be removed for the reaction front to propagate further, the reaction (7.5) probably becomes the rate limiting step on the silica-covered surface. Thus, the prerequisite of highest E_{act} for the rate determining step can be overruled by a lower pre-exponential factor for the process, here interpreted as the probability for water to find the right pore in the silica film to desorb. On the other hand, the accumulation of water due to its slow removal results in enhanced probability of reaction (7.4) providing an additional reaction pathway for OH formation. It is, therefore, tempting to assign the difference between two systems to confinement of water molecules leading to enhancement of self-dissociation reaction.

Certainly, further elaborative studies have to be done in order to understand chemical reactions at the bilayer silicate/metal interface, which may open new perspectives for rational design of catalytic hybrid materials combining molecular sieve and confinement effects.

7.4 Metal Deposition

In the next parts of this chapter, we consider adsorption of metals on ultrathin silica films. It is fair to say that the preparation of thin silica films on metals in early days was to a larger extent motivated by making them as suitable oxide supports for metal nanoparticles to model highly dispersed metal catalysts. It is also worth mentioning that first experiments on metal deposition onto ultrathin silica films were carried out even before their atomic structure has been established. Although metal deposits on ultrathin oxide films often showed adsorption characteristics identical to metal nanoparticles supported on oxide single crystals, it was realized that individual metal atoms may migrate into the ultrathin films. There is a growing body of experimental results showing that this phenomenon is related to the thickness of an oxide film rather than its nature. It is needless to say that metal deposition onto ultrathin silica may become a critical issue while considering possible applications of such films in nanoelectronics.

7.4.1 Metal Adsorption on a Monolayer Silicate

The initial stages of metal deposition on single layer silicates have been studied for Pd, Ag and Au on $SiO_{2.5}$/Mo(112) films. In order to minimize diffusion processes, the deposition and STM imaging were carried out at low temperatures. Figure 7.10 displays typical STM images of Pd and Au deposited and recorded at 10 K. The Au atoms form small clusters decorating antiphase domain boundaries in the film. In contrast, Pd-associated species are found randomly distributed, and they are imaged as weakly protruding hexagons on the atomically flat honeycomb-like surface. The absence of large single "blobs" suggests that the Pd atoms most likely reside below the surface, implying their migration into the silica layer even at cryogenic temperatures.

The ability of metal atoms to penetrate the silicate layer was examined by DFT by Pacchioni and co-workers.[16,17] It has turned out that a Pd atom easily, in essence barrierless, goes through the six-membered silica ring and strongly binds to the Mo atoms as depicted in Fig. 7.10. A driving force is obviously a much higher adsorption

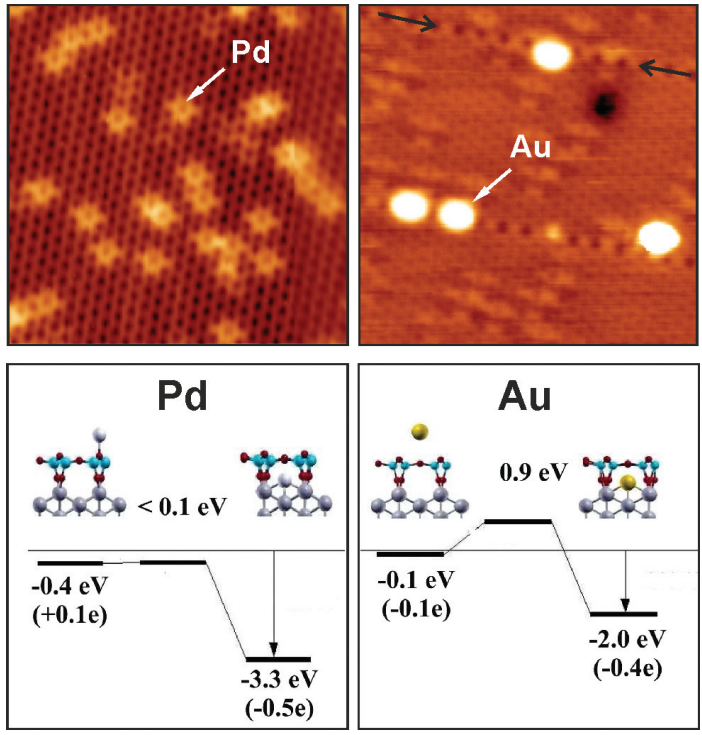

Figure 7.10 Low-temperature STM images of Pd (on the left) and Au (on the right) atoms deposited onto $SiO_{2.5}$/Mo(112) film at 10 K. Black arrows mark antiphase domain boundary. Adapted with permission from ref. 15. Below the images are the DFT-derived energies for Pd and Au atoms on and inside the silicate film with respect to a gas-phase atom. The associated energy barrier is also given. The values in parenthesis show the charge transfer from corresponding atom. Mo, dark gray; Si, cyan; O, red spheres; Pd, light gray; Au, yellow. Adapted with permission from ref. 16.

energy on metal than on silica, i.e., 3.3 and 0.4 eV, respectively. The potential energy profiles are found similar for both the six- and eight-membered rings, thus explaining uniform distribution of the Pd atoms on the films as observed by STM. Basically, every Pd atom that sticks to the surface becomes trapped in the silica ring. For comparison, an Au atom exhibits a considerably high activation barrier (0.9 eV) for a perfect silicate layer, despite a large energy gain (2 eV), albeit smaller than for Pd (3.3 eV). The barrier is, however,

substantially reduced for the eight-membered ring. Therefore, at low temperatures, the Au atoms only penetrate large rings available on antiphase domain boundaries consisting of alternating four- and eight-membered rings. Interestingly, further calculations revealed the eight-membered rings large enough to accommodate more Au atoms, thus forming dimer and trimer. To distinguish those by STM is not a trivial task, and required imaging at different tunneling conditions in combination with DFT-based image simulations.[17]

Intuitively, one may think of the observed "molecular sieve" effect is related to the metal atom size, that is, the smaller the atom, the more easily it penetrates the silica ring. Indeed, van der Waals radius of Pd (163 pm) is smaller than of Ag (172 pm). However, the calculated barrier for Au penetration (0.9 eV) is substantially higher than for Ag (0.3 eV), although its radius (165 pm) is smaller (because of the relativistic contraction of Au orbitals) and comparable with that of Pd. Therefore, the penetration probability does not seem to correlate directly with the effective size of the atom, but depends on its electronic structure. The calculations showed that the half-filled Ag 5s and Au 6s orbitals during penetration experience a substantial repulsion with the surface O 2p orbitals, thus leading to a higher barrier. In contrast, the unfilled Pd 5s orbital produces only a small repulsion. The much lower barrier for Ag in comparison with Au is attributed to a positive charging of the Ag atom in the transition state while passing the ring plane. The Ag atom transfers some charge into the Mo states, thereby reducing the electron–electron interaction with the oxide states. Being strongly electro-negative, the Au atom remains neutral when passing the silicate ring, and the repulsive interaction with the oxide surface electrons cannot be weakened. The Pd atom remains neutral during penetration, but becomes partly negatively charged in its final binding configuration.

The above scenario holds true solely for the "O-poor" films. The energetics considerably alters in the presence of O ad-atoms on the Mo support in the "O-rich" films as they occupy the sites the metal atom would otherwise adsorb on. In this case, the Pd adsorption energy decreases substantially, from 3.3 eV on the "O-poor" film to 0.7 eV on the "O-rich" film, although the activation barrier is almost unaffected. Therefore, to minimize or even suppress metal migration one should expose the films to oxygen prior to the metal deposition.

Once a metal atom has been migrated to the interface, it may act as an anchor for the next incoming atoms to form metal clusters. The deposition temperature and flux often influence the nucleation-and-growth process. At relatively high amounts of metal deposited, hemi-spherical nanoparticles form, as shown in Fig. 7.11a for the case of Pd deposited at room temperature. Adsorption of CO as a probe molecule for Pd revealed TPD and IRAS fingerprints of the clean Pd surface. Therefore, relatively large Pd aggregates formed on monolayer silica films are similar to those obtained on "thick" silica films and crystals, unless the sample is not heated to elevated temperatures inducing Pd migration into the film.

Interestingly, the particle size distribution considerably alters if Pd deposition is performed in the CO atmosphere. STM image in Fig. 7.11b shows that Pd particles deposited at 90 K and exposed

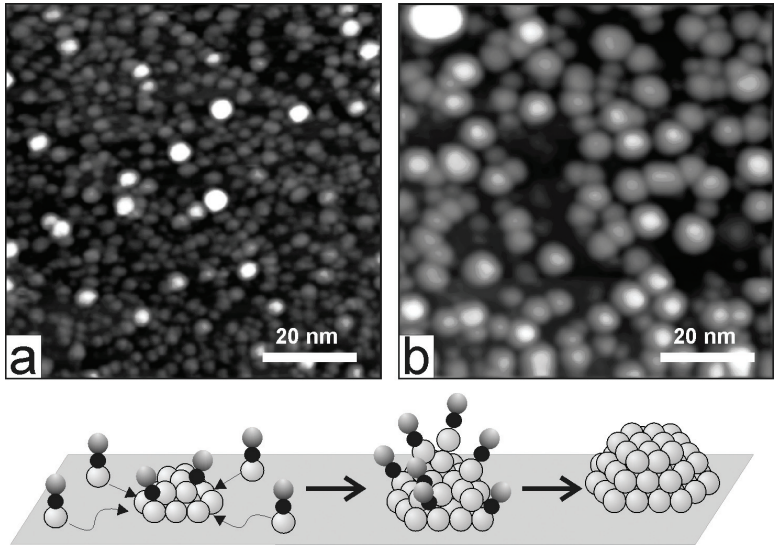

Figure 7.11 STM images of Pd particles on $SiO_{2.5}$/Mo(112). For image (a), Pd was deposited at 300 K; (b) The same amount of Pd was deposited at 90 K following adsorption of 20 L CO and heating to 300 K. CO-induced growth of Pd particles: CO adsorbs on Pd ad-atoms forming Pd carbonyls which diffuse and stick together forming a large agglomerate which decomposes upon heating and transforms into a metallic Pd particle. Adapted with permission from ref. 18.

immediately to CO and then heated to 300 K in UHV are substantially larger than the particles directly formed in UHV at 300 K (Fig. 7.11a). The effect can reasonably be rationalized by that CO molecules strongly adsorb on the Pd ad-atoms and small clusters formed at low temperatures as well as on the Pd atoms migrated into the film. Based on DFT predictions, the carbonyl PdCO complexes can even escape the silica cage, diffuse on the surface, and form aggregates. Monitored by TPD, CO desorbs from Pd carbonyl aggregates at about 200 K, resulting in larger Pd nanoparticles with CO still residing in multi-coordinated sites on the particle facets. Those species desorb on heating to 500 K.

Finally, the interaction of alkali metals with monolayer silicate films on Mo(112) has been studied using Li as an example.[19] As in case of Pd, the Li atoms readily penetrate the silicate layer and bind to the metal surface. Moreover, an ordered superstructure was found at increasing coverage seen as alternated stripes with high and low density of Li atoms along the particular direction on Mo(112). On the basis of the DFT calculations, the effect was explained in terms of the anisotropic screening response of the Mo(112) surface to Li adsorption. The Li atoms become positively charged and substantially lower the work function, which was measured by conductance spectroscopy.

7.4.2 Metal Adsorption on Bilayer Silica Films

In the same manner, the initial stages of metal adsorption were investigated for bilayer silicate films. It was reasonably expected that deposition at cryogenic temperatures (5 K) will only result in "monomeric" ad-species. Indeed, STM inspection revealed single atoms, however, not as individual protrusions, but as spots of a butterfly (crescent) shape (see Fig. 7.12). Again, there are some differences how Pd and Au deposits look in STM images. The Pd-related protrusions are more or less randomly distributed across the surface, whereas Au-related species are only found within the amorphous portions of the film and/or at domain boundaries, which obviously possess larger silica rings than in the crystalline film.

As in case of Pd on monolayer films, solely STM appearance of Pd species favors its assignment to an atom located underneath

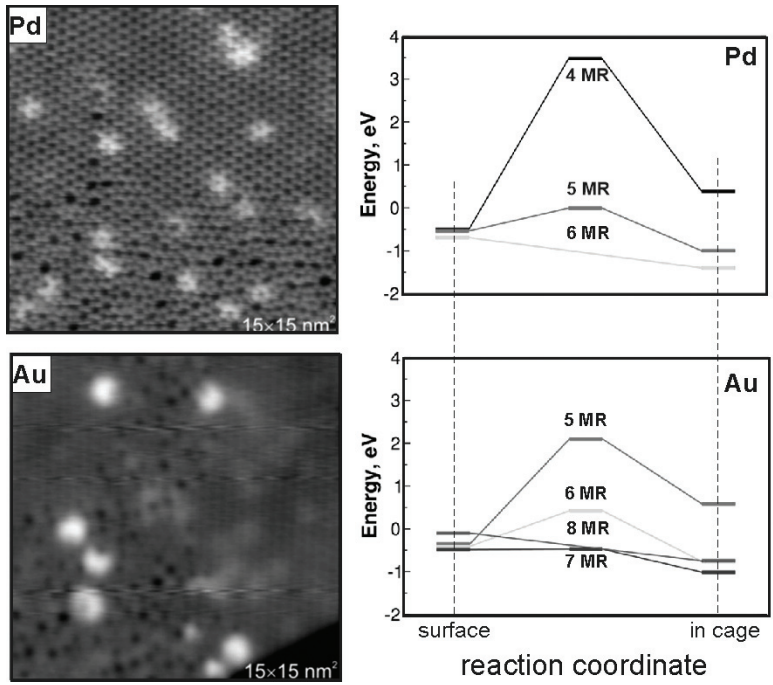

Figure 7.12 On the left: STM images of Pd and Au atoms deposited onto a bilayer silica film at 5 K. On the right: Energy profiles for Pd and Au penetrating the bilayer silica rings of different size ($n = 4$–8) computed for unsupported cluster models. Energies are calculated with respect to the metal atom in the gas phase. Adapted with permission from ref. 20.

or inside the film rather than on top. Indeed, DFT calculations predict the Pd atom to penetrate the hexagons without any barrier, thus making no significant difference for Pd adsorbed either on crystalline or amorphous portions. In contrast, the Au atoms only diffuse through the rings larger than heptagons existing in amorphous films and domain boundaries between the crystalline domains.

To gain more insight into metal interaction with silicate films, in particular whether metal atoms do migrate to the metal support, XPS measurements were carried out.[20] The idea behind is quite simple. As previously shown, adsorption of gas molecules on the metal surface underneath the film is accompanied by simultaneous

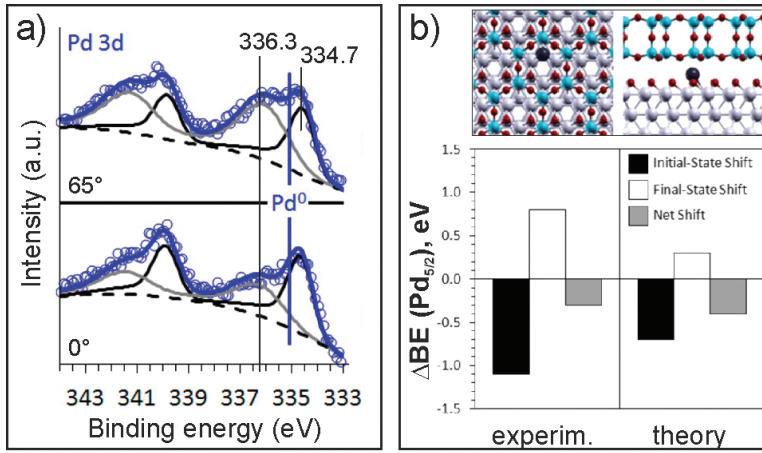

Figure 7.13 (a) Pd 3d region in XP-spectra measured for 0.05 ML Pd at two emission angles (65° and 0°) relative to the surface normal. Pd^0 marks the position of the $3d_{5/2}$ line for the Pd(111) crystal surface. (b) Experimentally detected change to the 3d BE, relative to bulk, (in gray) is partitioned into two contributions attributed, respectively, to changes in the initial- (black) and final-state (white) configurations of the photoemission process. Inset shows top and side views of a Pd atom bound at the interface between the bilayer film and the O-covered Ru(0001) substrate. Adapted with permission from refs. 20, 21.

shifts of the Si 2p and O 1s core levels due to the band re-alignment caused by the work function changes (see Chapter 4). Therefore, one anticipates such a shift also in case of metal atoms migrating to the support. Indeed, the measurements observed both levels shifted to higher binding energies (BE), by 0.3 and 1.2 eV after deposition of 0.05 and 0.24 ML of Pd, respectively. These shifts are actually equal to the work function changes (−0.3 and −1.2 eV, respectively) directly measured in the same experiments. However, the Pd 3d level showed a broad signal which was deconvoluted into two Pd states having BE higher and lower than that of measured on a Pd(111) single crystal, marked as Pd^0 in Fig. 7.13a. Relative intensity of the high BE component (at 336.3 eV) considerably increases at grazing emission, pointing to its surface origin. It is also qualitatively consistent with BE shifts typically observed for metal nanoparticles supported on thick oxide films and single crystals and attributed to

the "final state" effect caused by lack of screening of an electron hole in the photoemission process (see Chapter 2). Taking into account the relatively high deposition temperature (150 K) in these experiments that favors metal penetration through the film, the low BE signal in spectra (at 334.7 eV) can accordingly be assigned to the Pd atoms at the interface.

Of course, evaluation of XPS shifts associated with supported metal clusters or atoms on ultrathin oxide films is not straightforward because of a number of initial and final state effects such as charge transfer, size-dependent screening, electrostatic charging, lattice contraction which may even cause shifts in opposite directions and hence cancel each other. As introduced in Chapter 2, some of these contributions can be disentangled using the Auger parameter, which consists of the difference between the kinetic energies (KE) of XPS and Auger peaks from the same atom in a given material. In fact, more informative are the changes in Auger parameter when comparing the spectra for a given atom in different environment, in particular for the so-called modified Auger parameter ($\Delta\beta$), where the Auger measurement is limited to core-core-core lines with final states consisting of two holes in the same orbital probed by the XPS measurement. In our case of Pd, one should measure Pd 3d photoelectron lines and the $L_3M_{45}M_{45}$ Auger transition lines. Accordingly, analysis of the silica states includes $K_1L_{23}L_{23}$ Auger transition to complement the Si 2p photoelectron line. As the energy needed to excite these Auger transitions (1600–3200 eV, depending on the element) exceeds that of conventional x-ray sources, the inherent Bremsstrahlung radiation was used to probe the specified Auger peaks.

Applying Auger parameter by comparing the change in the KE of the Si $K_1L_{23}L_{23}$ Auger peaks to determine energy contributions for the final-state relaxation showed that the latter is negligible. In fact, the O 1s and Si 2p BE shifts solely follow the work function. Any changes to the system that result in a decreased (increased) work-function will always decrease (increase) the energy of the band structure within the ultrathin silica film, i.e. in the same manner as was suggested for the "O-rich" versus "O-poor" film systems. The analysis applied to the Pd adsorption, summarized in Fig. 7.13b, showed that the negative shift of BE by 0.3 eV, relative

to the Pd 3d peak position in the bulk, should be attributed to large variations in the initial-state orbital energies of the single atoms (1.1 eV towards the Fermi level), which is large enough to overcome decreased final-state relaxation contributions (0.8 eV), ultimately yielding the net-negative 0.3 eV shift measured by XPS. The conclusion was nicely supported by theoretical calculations, also presented in Fig. 7.13b.

Theoretical considerations were further expanded to the cases of adsorptions of Li, Na, K, and Mg, not yet experimentally studied. Basically, the idea was to check whether alkali and alkaline-earth metal atoms and ions can be stabilized in the small cages provided by the bilayer Al-silicate representing a two-dimensional model of zeolites. To reduce computational costs, the unsupported cluster models were only employed, all shown in Fig. 7.14. According to the calculations, no charge transfer takes place between silica and adsorbed atom which remains metallic. The interaction is dominated by dispersive forces. As the ring size increases, the stability of the atoms inside the cages enhances, but is still unfavorable for all the ring sizes studied. Interestingly, the adsorption energy does not follow any regular trend like in the Periodic Table, e.g., going from Li, to Na and to K. In fact, for the hexagonal ring, it is largest for K, and smallest for Na, with Li in an intermediate position (-0.53, -0.37, and -0.45 eV, respectively). This is the result of two different factors affecting the bonding. On the one hand, there is the atomic polarizability that is largest for heavier atoms (K $>$ Na $>$ Li). On the other hand, the atomic dimension favors a stronger interaction for the lighter atoms (Li $>$ Na $>$ K).

The interaction becomes stronger when one Si atom in the cluster model (indicated by the arrow in top panel of Fig. 7.14) is replaced by Al to mimic zeolitic frames. This has an enormous effect on the adsorption energies of Na atom, which increases by an order of magnitude, i.e., from 0.3 to 4 eV. As a result, Na is positively charged (Na^+), and electrostatic interaction starts to dominate the adsorption process, albeit it still depends on the ring size. For large rings, the Na ion ultimately occupies sites in vicinity to the Al ions in the framework.

Not surprisingly, the situation changes substantially for the metal supported films. The alkali metals all become thermodynamically

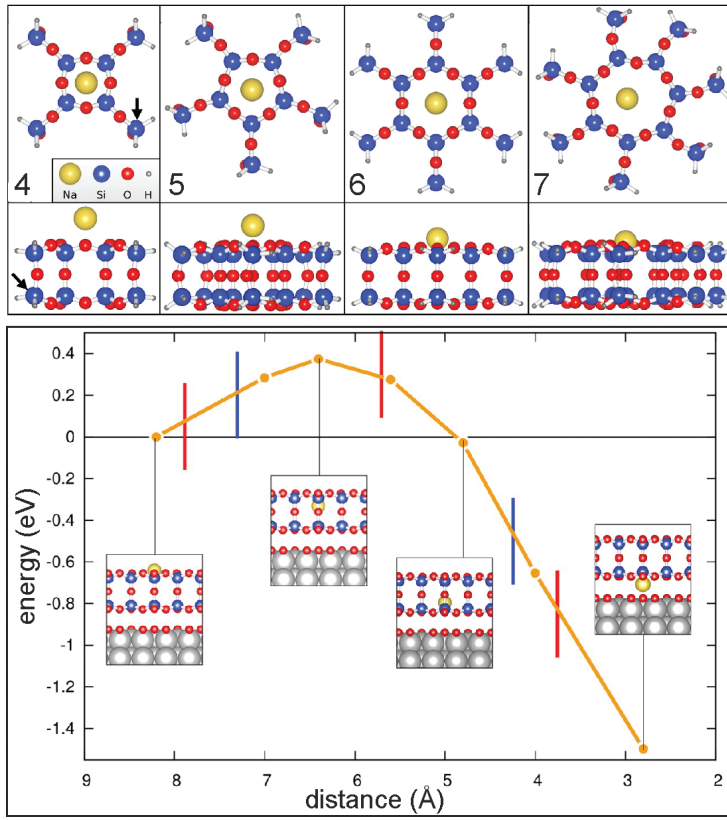

Figure 7.14 Top panel: Top and side views of the optimized geometry of a Na atom interacting with a cluster model mimicking N-membered rings ($N = 4$–7). The arrow marks the Si atom that was replaced by Al to mimic aluminosilicate frame in separate calculations. Bottom panel: Potential energy curve for the diffusion of a Na atom into the six-membered ring of the $SiO_2/3O(2\times2)/Ru(0001)$ films. The zero of energy corresponds to Na adsorbed on the surface of the film. The vertical bars indicate the position of the O (red) and of the Si (blue) layers. Adapted with permission from ref. 22.

the most stable if intercalated the interface. The energy profile only computed for six-membered ring is shown in the bottom panel of Fig. 7.14. Although the barrier (0.4 eV) does not correspond to a real transition state, it appears that the energy required for penetration can readily be overcome at moderate temperatures.

For larger rings present in the amorphous portions of the film, the barrier is presumably smaller. Upon reaching the metal surface the Na atom experiences charge transfer and become Na^+. Noteworthy, the distance between the silica film and the metal support upon alkali metal adsorption does not change, as it was the case for CO and oxygen gas adsorption studied in the previous sections (see Fig. 7.5).

As a consequence of the metal diffusion to the interface, the calculated work function decreases substantially, i.e., by 1.1 eV (for Na) and 1.3 eV (for Mg). Note, however, that the work function changes may even be by 1–1.5 eV higher, if Na(Mg) ions could be stabilized at the surface. Such a strong reduction of the work function by alkali metal adsorption may have a strong impact on the subsequent adsorption of gaseous molecules. This is interesting issue that has to be studied in the future.

References

1. Sutter, P., J. T. Sadowski, and E. A. Sutter, Chemistry under cover: Tuning metal–graphene interaction by reactive intercalation. *Journal of the American Chemical Society*, 2010. **132**(23): pp. 8175–8179.
2. Over, H., and M. Muhler, Catalytic CO oxidation over ruthenium—bridging the pressure gap. *Progress in Surface Science*, 2003. **72**(1–4): pp. 3–17.
3. Emmez, E., et al., Oxidation of the Ru(0001) surface covered by weakly bound, ultrathin silicate films. *Surface Science*, 2016. **646**: pp. 19–25.
4. Zhong, J.-Q., et al., Oxidation and reduction under cover: Chemistry at the confined space between ultrathin nanoporous silicates and Ru(0001). *The Journal of Physical Chemistry C*, 2016. **120**(15): pp. 8240–8245.
5. Emmez, E., et al., Permeation of a single-layer SiO_2 membrane and chemistry in confined space. *The Journal of Physical Chemistry C*, 2014. **118**(50): pp. 29034–29042.
6. Pfnür, H., et al., High resolution vibrational spectroscopy of CO on Ru(001): The importance of lateral interactions. *Surface Science*, 1980. **93**(2–3): pp. 431–452.
7. Schlexer, P., et al., CO adsorption on a silica bilayer supported on Ru(0001). *Surface Science*, 2016. **648**: pp. 2–9.

8. Tissot, H., et al., Ultrathin silica films on Pd(111): Structure and adsorption properties. *Surface Science*, 2018. **678**: pp. 118–123.
9. Guo, X., and J. T. Yates, Dependence of effective desorption kinetic parameters on surface coverage and adsorption temperature: CO on Pd(111). *The Journal of Chemical Physics*, 1989. **90**(11): pp. 6761–6766.
10. Gdowski, G. E., T. E. Felter, and R. H. Stulen, Effect of surface temperature on the sorption of hydrogen by Pd(111). *Surface Science*, 1987. **181**(3): pp. L147–L155.
11. Yao, B., et al., Gas separation through bilayer silica, the thinnest possible silica membrane. *ACS Applied Materials & Interfaces*, 2017. **9**(49), 43061–43071.
12. Zhong, J.-Q., et al., Immobilization of single argon atoms in nano-cages of two-dimensional zeolite model systems. *Nature Communications*, 2017. **8**: p. 16118.
13. Prieto, M. J., et al., Water formation under silica thin films: Real-time observation of a chemical reaction in a physically confined space. *Angewandte Chemie International Edition*, 2018. **57**(28): pp. 8749–8753.
14. Kostinski, S., et al., Diffusion of water molecules in amorphous silica. *IEEE Electron Device Letters*, 2012. **33**(6): pp. 863–865.
15. Baron, M., et al., Adsorption of Au and Pd atoms on thin SiO_2 films: The role of atomic structure. *The Journal of Physical Chemistry C*, 2008. **112**(9): pp. 3405–3409.
16. Ulrich, S., et al., Realization of an atomic sieve: Silica on Mo(112). *Surface Science*, 2009. **603**(8): pp. 1145–1149.
17. Ulrich, S., et al., Evidence for a size-selective adsorption mechanism on oxide surfaces: Pd and Au atoms on SiO_2/Mo(112). *ChemPhysChem*, 2008. **9**(10): pp. 1367–1370.
18. Lu, J. L., et al., Structure, thermal stability, and CO adsorption properties of Pd nanoparticles supported on an ultra-thin SiO_2 film. *Surface Review and Letters*, 2007. **14**(5): pp. 927–934.
19. Jerratsch, J. F., et al., Lithium incorporation into a silica thin film: Scanning tunneling microscopy and density functional theory. *Physical Review B: Condensed Matter and Materials Physics*, 2009. **80**(24): p. 245423.
20. Büchner, C., et al., Adsorption of Au and Pd on ruthenium-supported bilayer silica. *The Journal of Physical Chemistry C*, 2014. **118**(36): pp. 20959–20969.

21. Kaden, W. E., et al., Understanding surface core-level shifts using the Auger parameter: A study of Pd atoms adsorbed on ultrathin SiO_2 films. *Physical Review B*, 2014. **89**(11): p. 115436.
22. Schlexer, P., L. Giordano, and G. Pacchioni, Adsorption of Li, Na, K, and Mg atoms on amorphous and crystalline silica bilayers on Ru(0001): A DFT study. *The Journal of Physical Chemistry C*, 2014. **118**(29): pp. 15884–15891.

Chapter 8

Water Adsorption on Silica Films

The interaction of water and silica, the two most abundant compounds on our planet, has always been a subject of research interest in the course of the formation and development of natural sciences, and it covers a wide variety of scientific disciplines. Water/silica reactions play a decisive role in natural processes such as weathering and dissolution. The performance of silica in catalysis largely depends on the density and spatial distribution of hydroxo species at surface. Everyone opening boxes with new household items has seen small bags filled by silica gel granules as drying agent.

Since this book highlights the "surface science" approach to understanding the structure and properties of silica and related materials, it is fair to mention here Thiel and Madey's review paper from 1987[1] summarizing experimental studies of water interaction with metal and oxide surfaces primarily carried out on single crystals. Although the review has been updated and extended by Henderson in 2002,[2] these reviews provide, in fact, not so much information about silica. It is because of (i) well-known difficulties to prepare clean surfaces of silica single crystals, and (ii) insulating properties of silicas, that makes the experimental studies quite difficult and renders the results often uncertain.

Spectroscopic techniques such as nuclear magnetic resonance spectroscopy, infrared and Raman spectroscopy are primarily used

Introduction to Ultrathin Silica Films: Silicatene and Others
Shamil Shaikhutdinov

ISBN 978-981-4877-28-2 (Hardcover), 978-1-003-08862-2 (eBook)
www.jennystanford.com

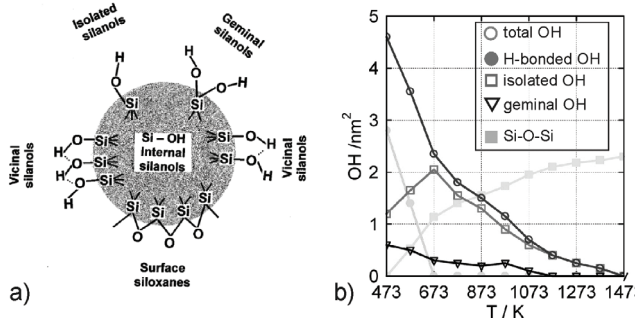

Figure 8.1 (a) Types of silanol groups on amorphous silica. Adapted with permission from ref. 3. (b) Distribution of the surface OH groups as a function of the treatment temperature. Adapted with permission from ref. 4.

for investigating hydrated silicas. Numerous results from these studies suggested the presence of isolated silanols (i.e., single silanols, Si–OH, and geminal silanols, Si–$(OH)_2$) and hydrogen-bonded silanols at surface (Fig. 8.1). Statistical analysis of hydrated silica materials by Zhuravlev[3] led him to conclude that the maximum density of silanol groups on a hydroxylated surface amounts to about 5 OH per nm^2 irrespectively of the preparation method and silica morphology.

It is generally accepted that water chemisorbs by opening strained siloxane (Si–O–Si) bonds at surface resulting in two silanol groups as schematically shown below. Subsequent water molecules bind to existing silanols via hydrogen bonds rather than adsorb molecularly on the pristine siloxane surface.

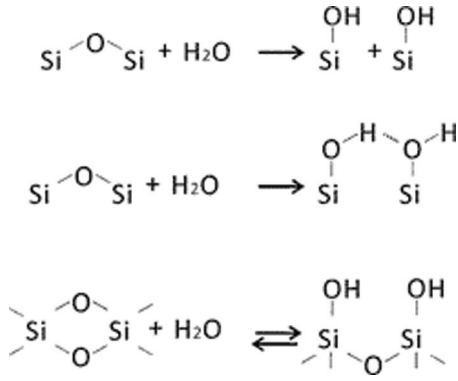

Early theoretical works addressing water/silica interfaces have been performed using cluster calculations, in particular to understand the atomic structures of various hydroxyl species. Significant progress has been achieved by employing density functional theory (DFT). Note, however, that weak interactions, such as hydrogen bonds, are notoriously difficult for DFT methods to implement accurately. The accuracy of a given functional may depend on the choice of basis set. For obvious reasons, calculations have first been performed on the crystalline surfaces, mainly of quartz.

Dissociative adsorption at the (0001), (10-10), (10-11), and (10-1-1) surfaces of α-quartz is energetically favorable, as it results in the large adsorption energies and lowering the surface energies.[5] However, water molecules do not adsorb on the reconstructed, siloxane (Si–O–Si)-terminated α-quartz(0001) surface (for its surface structure, see Fig. 1.12 in Chapter 1). DFT analysis of layer-by-layer water adsorption on the clean reconstructed as well as hydroxylated α-quartz (0001) surfaces showed that, except the case of monolayer adsorption, the interaction between water molecules and bare quartz surfaces with Si–O–Si termination is relatively weak. The interaction with the hydroxyl-terminated surface is much stronger. A stable water bilayer may be formed on both surfaces as illustrated in Fig. 8.2b.

In experiments, however, the initially OH-free silica surfaces are usually obtained by dehydroxylation of silicas via vacuum annealing at elevated temperatures. DFT analysis of this process for the (001), (101), and (111) surfaces of β-cristobalite[7] suggested complex surface reconstruction involving silica units migration. The latter was required to reach the experimentally measured values for hydroxyl coverage (3.7–5.2 OH/nm^2 in standard conditions, see Fig. 8.1b) despite obvious topological differences between ordered model structures used in calculations and amorphous silica samples used in experiments.

The results for the Si–O–Si reconstructed quartz surface can, in principle, be adopted for water adsorption on natural sheet silicates. Molecular dynamics simulations on mica (muscovite) showed that, at monolayer coverage, water forms a fully connected two-dimensional H-bond network like a "two-dimensional ice" depicted in Fig. 8.3.[8] The structure is predicted to be stable at

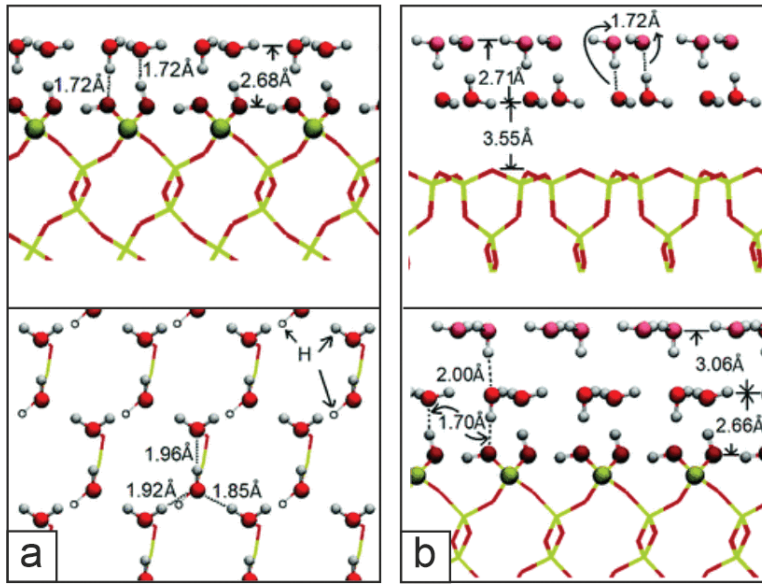

Figure 8.2 (a) Side and top views of water monolayer on fully hydroxylated quartz (0001) surface. (b) Cross views of water bilayer formed on the siloxane-terminated (top) and hydroxylated (bottom) quartz (0001) surfaces. Adapted with permission from ref. 6.

300 K, and as such it may explain the ordered structure observed by atomic force microscopy (AFM) on the hydrated mica surface at room temperature.[9] Also, AFM images of mordenite (one of the most abundant high-silica zeolite minerals) indicated an alignment of hydroxyl groups on both the (010) and (100) surfaces.[10]

In the following sections, we will discuss water adsorption on thin silica and related films primarily by infrared spectroscopy, which remains the principal technique for studying water interaction with silica.

8.1 Water Adsorption on a Monolayer Film

First studies of water adsorption on single-layer silicate films grown on Mo(112) were performed using high-resolution electron

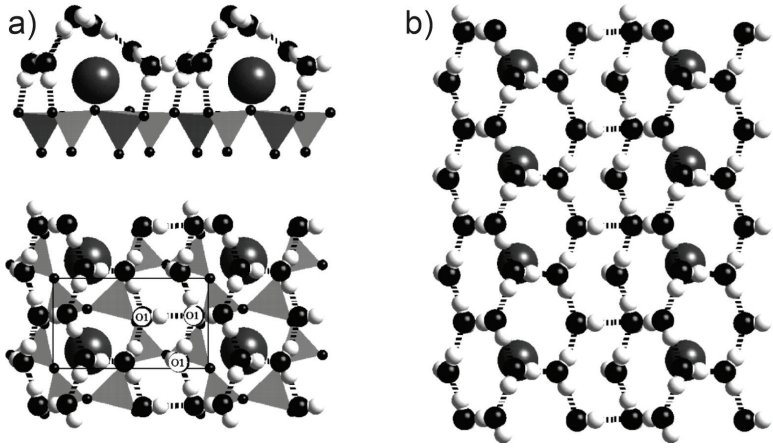

Figure 8.3 (a) The optimized structure of water monolayer on mica in side and top views. Dashed lines are hydrogen bonds. The unit cell of the 2D-ice structure, which coincides with the unit cell of mica, is indicated. There are six water molecules per unit cell; half of them (denoted by O1) are bound to the surface oxygen atoms. The other water molecules solvate the potassium ions, and form bonds to the underlying water molecules and to each other. (b) Top view of the 2D-ice structure, where only the K ions of the mica surface are shown. The H-bonds network consists of distorted hexagons. Reproduced with permission from ref. 8.

energy loss spectroscopy (HREELS).[11] The results suggested the formation of three-dimensional water clusters at low temperatures which desorb intact upon heating, leaving no surface hydroxyls behind. Our own infrared reflection absorption spectroscopy (IRAS) studies[12] confirmed growth solely of so-called "amorphous solid water" (ASW) film. (NB: One should discriminate ASW from ice, which is a crystalline form of water, although the "ice" is frequently used for brevity.) Accordingly, water desorption follows zero-order desorption kinetics showing the common leading edge in temperature programmed desorption (TPD) spectra, with a maximum gradually shifting to the higher temperature at increasing coverage. However, dosing H_2O at 140 K, i.e., very close to the onset of water desorption ($\sim$145 K), results in a pseudo-first order kinetics (i.e., the signal intensity scales with the coverage, but the maximum peak does not shift). Interestingly, water dosed at 140

K desorbed at temperatures by 7 K higher than the same amount of water dosed at 100 K. Even a larger difference (18 K) was observed for deuterated water (D_2O). It should be mentioned that for systems dominated by weak H-bonding such differences are quite substantial.

The IRAS spectra recorded during slow heating of the water film from 100 to 140 K considerably alter, even though water is not desorbing at these temperatures. This phenomenon is well-documented for other substrates and commonly interpreted in terms of the ASW-to-ice transformation.[13] Looking in the region of silica phonons, a slight blue-shift (9 cm^{-1}) of the principal band at 1060 cm^{-1} was observed upon water adsorption at 100 K as the ASW film, i.e., with the water molecules randomly oriented with respect to the silica surface. The formation of the ice-like layer (at 140 K) results in a much larger (by 20 cm^{-1}) shift. The experiments with the silica film prepared with the ^{18}O isotope confirmed that this effect originates from the water/silica interface. Since water is a polar molecule having a large dipole moment, the observed shifts are most likely caused by polarization of the water/silica interface. As the shift is found larger for the ice-like layer, it suggests water reorientation with respect to the silica surface and hence some sort of ordering.

Indeed, temperature-programmed LEED measurements (i.e., recording LEED patterns during sample heating) revealed additional diffraction spots (Fig. 8.4a) shortly appearing at around 145 K, i.e., at temperature close to the desorption maximum in TPD spectra, suggesting that the corresponding ordered structure forms at relatively low water coverage. The observed pattern corresponds to the water ad-layer in c(2×2) symmetry with respect to the silicate layer, which is in turn form c(2×2) structure to Mo(112). That the same pattern is observed by water dosing directly at 145 K points to that water ordering is thermodynamically driven, not kinetically. (Certainly, in all LEED experiments one has to take precautions to ensure that the effect is not induced by the incident electron beam).

The formation of water ordered structures has been reported for noble metal surfaces using STM at low temperatures.[14,15] On the basis of the DFT calculations, it was assigned to a water layer like in the basal plane of the hexagonal *Ih* phase of ice. Basically, the

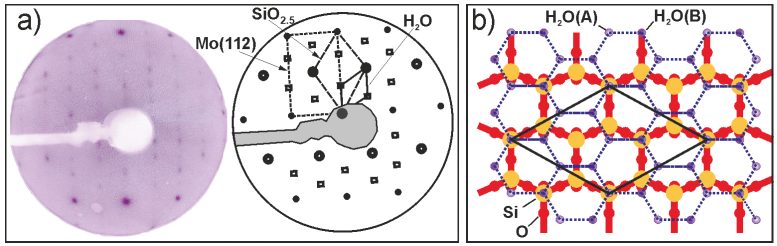

Figure 8.4 (a) LEED pattern of ordered water ad-layer on a $SiO_{2.5}$/Mo(112) film (in negative contrast) and its schematic presentation. The unit cells are only indicated for one rotational domain. (b) Top view of a structural model. H-bonding network of two differently oriented water molecules (A, B) within the bilayer structure of ice forms a c(2×2) superstructure (marked as rhomb) with respect to the silicate layer.

weakly adsorbed water molecules form a honeycomb-like network stabilized by hydrogen bonds (see also Fig. 8.2a). In the same manner, one can place the ice layer on top of a silicate film such that it fits the c(2×2) symmetry. The resulted model is depicted in Fig. 8.4b.[12] In this structure, there is a relatively small difference between the O—O distances in the ice *Ih* (2.61 Å, if projected onto the (0001) plane) and in the topmost O-layer of silicate (2.73 Å).

Such a possibility has been examined by DFT,[16] although the calculations were carried out for free-standing silicate bilayer in a slab containing a (1×1) unit cell, whereas water layer forms the c(2×2) structure. At low coverage (Fig. 8.5a), water molecules are isolated. The oxygen atom in the water molecule sits on top of the Si atoms, whereas the water protons are directed toward the siloxane oxygen atoms, but without forming a hydrogen bond. At higher coverages, two stable structures can be formed (Fig. 8.5b,c) in a H-bonding network resembling an ice-like arrangement. For three H_2O molecules per unit cell, the optimized structure contains water molecules coordinated in a distorted tetrahedral fashion, making interconnected six-membered and three-membered H-bonded water rings. The latter is absent in known forms of ice. In case of 2 H_2O/unit cell, the layer derived from the *ice XI* phase fits better the hexagonal rings of the silicate film. This latter model is a good candidate to explain the experimental observations. (Note again, however, that the calculations were performed for

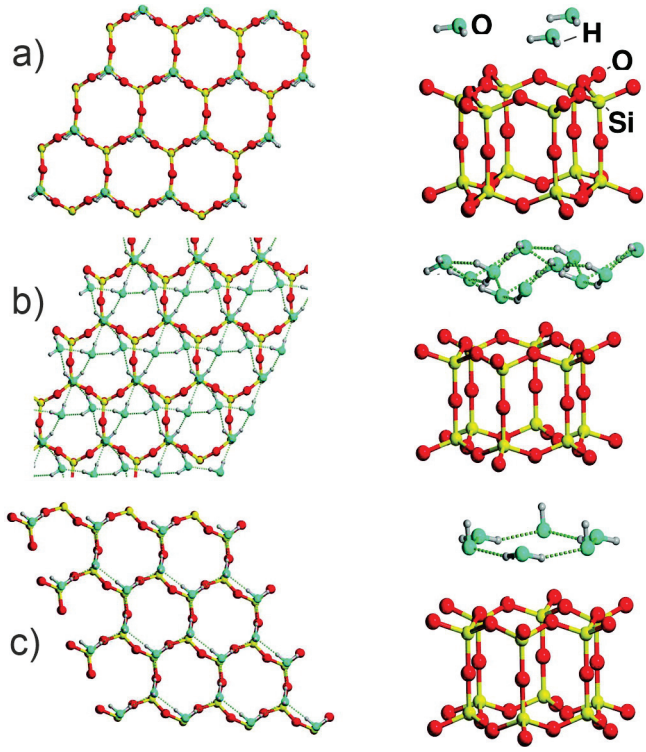

Figure 8.5 DFT-optimized structures of H_2O adsorbed on the free-standing silicate bilayer at low (a) and high (b,c) coverages. Adapted with permission from ref. 16.

the (1×1) unit cell). Nevertheless, the DFT results are consistent with the experimental finding of that water does not dissociate on the siloxane-terminated, silicate monolayer. Apparently, the water/water interaction is much stronger than the water/silica interaction.

We continue discussion of water interaction with a single silicate layer prepared on Ru(0001). Such films are considerably more defective than the crystalline films grown on Mo(112) (see Chapter 4). Therefore, one anticipates different reactivity of these two films towards hydroxylation. Indeed, IRAS inspection of the Ru-supported films exposed to water vapor at 100 K and then heated to 300 K to desorb the ASW film revealed a sharp band at

2760 cm^{-1} (see inset in Fig. 8.6b) reflecting O–D stretch vibration in silanols (Si–OD). (Henceforth, we primarily use D_2O instead of H_2O). Concomitantly, isolated protrusions about 1 Å in height appear in STM images, which can straightforwardly be assigned to surface hydroxyls. Only a few such species are observed on crystalline domains, while most of those are located at domain boundaries and at the rim of adventitious holes (Fig. 8.6a). Obviously, the surface hydroxylation under these conditions only takes place on defects. The latter are present in abundance on the same films annealed in UHV, forming a periodic defect structure (see Fig. 5.7 in Chapter 5). As a result, surface hydroxyls and their aggregates decorate the periodic defects (Fig. 8.6b). Trimers are reminiscent of triangular (T-) defects, while quatromers are definitely related to rectangular (R-) defects, both described in Chapter 5. Therefore, patterning defects on the silica surface would allow to control spatial distribution of surface hydroxyls on silica. The latter is important for anchoring catalytically active species in so-called "single atom catalysts".

Analysis of high-resolution STM images allowed to localize the position of silanols at surface as illustrated in Fig. 8.6c. The water-related protrusions are preferentially located above the Si atoms at the nodes formed by non-equivalent polygons, for instance, a pentagon, hexagon, and heptagon. Water adsorption experiments on the film prepared with $^{18}O_2$ showed no shift for the ν(OD) band at 2760 cm^{-1}, indicating that oxygen in silanols is only coming from the water, and no oxygen scrambling takes place. Therefore, the STM observation of hydroxyl on top of the Si atoms in defects suggests breaking of the SiO–Ru linkage which is followed by Si atom popping up to strongly bind OD from the water molecule that dissociates. In this scenario, the second D in the water should form another hydroxyl with the O atom in silica. However, the related band (that would definitely experience a shift in ^{18}O-labeled films) was never detected. The fate of the second H remains unknown. Either the respective hydroxyl is oriented parallel to the metal surface and hence becomes invisible due to the metal surface selection rules (Chapter 2) or this H atom migrates onto the metal surface.

One may argue that water adsorption on a single silicate layer is affected by its strong bonding to a metal substrate. In this respect, a bilayer silicate film weakly bonded to the metal surface is expected

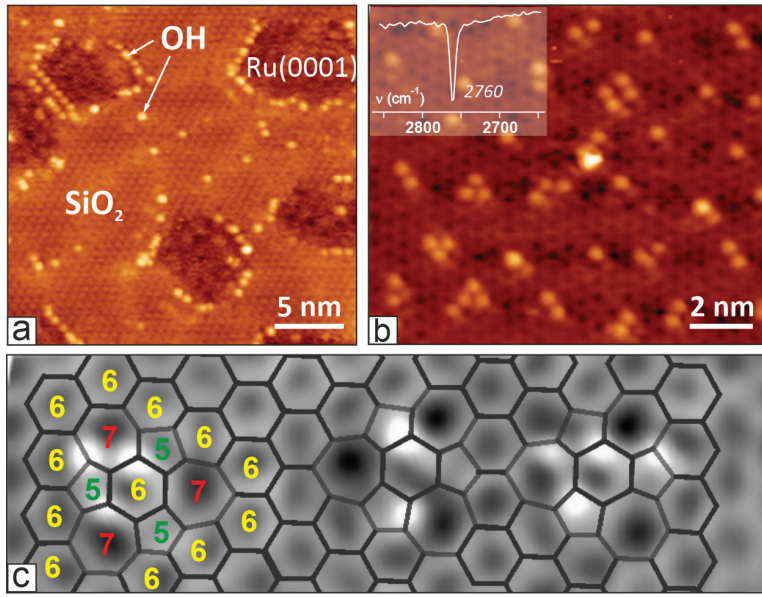

Figure 8.6 STM images of hydroxylated monolayer silicate films on Ru(0001) formed by water adsorption onto: (a) "as prepared" film; (b) UHV-annealed film showing periodic defects (see Figure 5.7 in Chapter 5). The inset in panel (b) shows typical IRAS spectrum in the OD stretch vibration region. (c) STM image superimposed with polygonal representation of silica rings. Adapted with permission from ref. 17.

to show some difference. In general, one could consider bilayer film as the more adequate system to study reactions of silica with water.

Water exposure under UHV-compatible conditions did not result in surface hydroxylation. Only tiny amounts of isolated hydroxyls are detected by IRAS via the 2763 cm^{-1} band.[18] Note that the band is only slightly blue-shifted when compared to a single silicate, suggesting that the OD vibration in surface silanols is sensitive to local Si coordination and not to surface ordering. The band disappears at heating at temperatures as high as 1000 K indicating a good thermal stability of silanols. Based on the signal intensity, the silanol density is in the order of 0.1 nm^{-2}, or about one hydroxyl per 40 silica rings. Such a small concentration points to the defect-mediated hydroxylation.

8.2 Electron Beam Assisted Hydroxylation

The results presented in the previous section are well consistent with anticipated inertness of the siloxane-terminated silica surfaces. However, to study the chemistry of silanols using planar model systems it is desirable to have them in substantial amounts. Moreover, one has to control the degree of hydroxylation in order to establish the relationship with their chemical activity. To promote the hydroxylation of our silicate films one needs to create defects. Under vacuum conditions this could be done, for example, by electron or ion bombardment. However, usage of ion bombardment is very tricky in the case of ultrathin films because of the obvious sputtering effects. On the other hand, electron irradiation of the pristine films showed negligible effects on subsequent water adsorption due to the presence of a metal support which efficiently quenches possible excitations induced by electron beam. Instead, we proposed another approach which is based on using electron irradiation of the silicate films covered by "ice" (Fig. 8.7).[19] The underlying idea is fairly simple: If high-energy electrons create short-living surface defects in silica, these can react immediately with surrounding water molecules more efficiently as compared to water post-dosing.

Electron bombardment of relatively thick ASW films causes, in essence, no effect on the amount of surface hydroxyls formed after subsequent heating of the bombarded sample to the room temperature to desorb unreacted water molecules. Apparently, ice

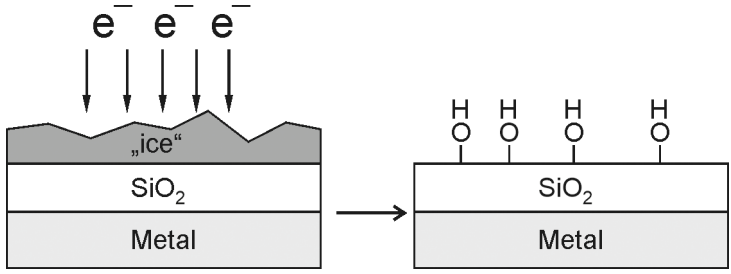

Figure 8.7 Schematic illustration of the silica hydroxylation assisted by electron irradiation of a solid water film.

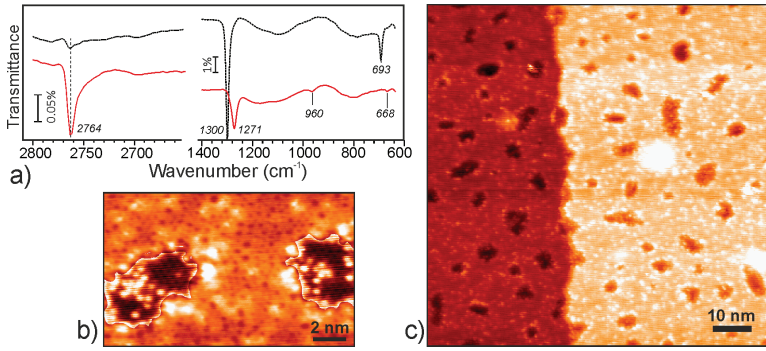

Figure 8.8 (a) IRAS spectra of the SiO_2/Ru(0001) surfaces hydroxylated without (dash line) and with (solid line) low-energy electron irradiation of the ASW film at 100 K. Both samples were heated in UHV to 300 K before recording the spectra at 100 K. Adapted with permission from ref. 19. (b,c) STM images of hydroxylated surfaces prepared with electron irradiation. The dark spots in these images are monolayer silicate domains initially presented in the sample as shown in image (b) presented in differentiated contrast.

overlayer must be of thickness comparable with the electron mean free path and/or exciton diffusion length in ice. In fact, low-energy electrons (100–500 eV) efficiently sputter the ice film, since the related IRAS bands attenuate at increasing beam exposure time. In practice one exposes the sample to water at low temperatures to form a relatively thick ASW film solely to ensure its uniform coating, and then irradiates with electrons until the water film is almost sputtered. After desorption of remaining water molecules by thermal flash in vacuum, IRAS spectra show a much higher concentration of hydroxyls (see Fig. 8.8a) as compared to the silica film similarly treated, but without electron irradiation. At such high concentration even a much weaker band at 960 cm^{-1} associated with Si–O bond stretch vibrations in silanols becomes clearly observed.

Using the results on a hydroxylated single layer silicate film for calibration, with the silanol density being directly measured by STM (see Fig. 8.6), the observed IRAS signals correponds to the amount of silanols occupying about 10% of all the Si atoms in the top silicate layer. (Note that such an estimate does not account for hydroxyls,

if any, oriented parallel to the surface and hence "invisible" for IRAS due to the metal selection rules). The silanols are thermally very stable and disappear from the surface via water desorption on heating to 900 K and above, i.e., at considerably higher temperatures as compared to the monolayer silicate (~700 K). It appears that strong interaction of monolayer films with a metal support provides additional pathway for hydroxyls desorption as water.

The surface hydroxylation leads to strong attenuation of the silica phonon bands which in addition shift to the lower frequencies by a value roughly proportional to the degree of hydroxylation, but about 30 cm^{-1}, at most. Therefore, it is clear that the bilayer structure of the film remains. This is also confirmed by STM inspection of the hydroxylated films. Numerous white protrusions seen in Fig. 8.8c can be assigned to surface hydroxyls, which randomly cover the surface. There are in addition adventitious spots exposing the single-layer silicate (Fig. 8.8b) which look very similar to those observed upon hydroxylation of a monolayer silicate film (Fig. 8.6). The STM results could not yet precisely identify silanols position.

Following siloxane bond opening mechanism for hydroxylation (see the scheme in introduction), two hydroxyl species are formed. One includes oxygen from water (O_w) and another one incorporates oxygen from silica (O_s), both can be spectroscopically distinguished using isotopic labeling of oxygen in the water and/or the silica. The experiments on the films prepared with $^{18}O_2$, indeed, showed two bands, at 2764 and 2746 cm^{-1} (as shown in Fig. 8.9) which can be assigned to $^{16}O_wD$ and $^{18}O_sD$ species solely on the basis of a reduced mass analysis (the oscillator with the heavier mass exhibits the lower frequency). Also, the formation of silanols by atomic D, if the latter is produced by radiation, can be excluded as this would only result in a single O_sD band at 2746 cm^{-1}. Although the observation of the two OD bands agrees with the siloxane bond opening mechanism, resulting in two virtually identical hydroxyls, the bands behave differently on heating. Up to 700 K, the integral intensities of the bands stay fairly constant, but the bands become sharper. At further heating, the 2764 cm^{-1} signal attenuates, whereas the 2746 cm^{-1} band gains in intensity so that it becomes even larger than the 2764 cm^{-1} band. Both bands ultimately disappear upon heating to 1240 K. In addition, during heating the bands experience some

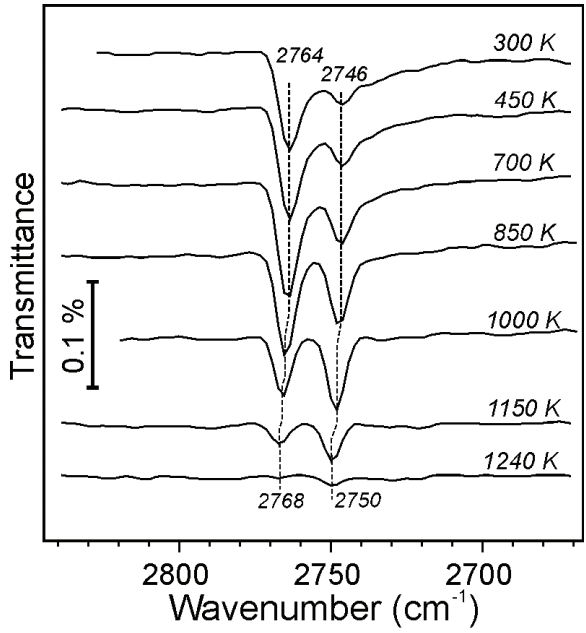

Figure 8.9 The ν(OD) spectra of the $Si^{18}O_2$ bilayer film, hydroxylated by using $D_2^{16}O$ water, as a function of annealing temperature. The hydroxylation was obtained with 150 V electron irradiation of the ASW film deposited at 100 K. Adapted with permission from ref. 19.

shift, albeit small. As already mentioned above, one has to bear in mind that the band intensity in IRAS depends also on the dipole orientation with respect to the metal surface and gets smaller when it becomes parallel to the surface. Therefore, the observed spectral changes may also reflect thermally induced structural relaxations.

Interestingly, the same two bands and the similar spectral evolution were observed for "thermally" hydroxylated films, i.e., without irradiation. The difference is only a substantially smaller signal intensity that implies a common mechanism for the surface hydroxylation. It appears that electron irradiation aids in overcoming the activation barrier which cannot be achieved thermally simply because water molecules desorb intact before the reaction could occur.

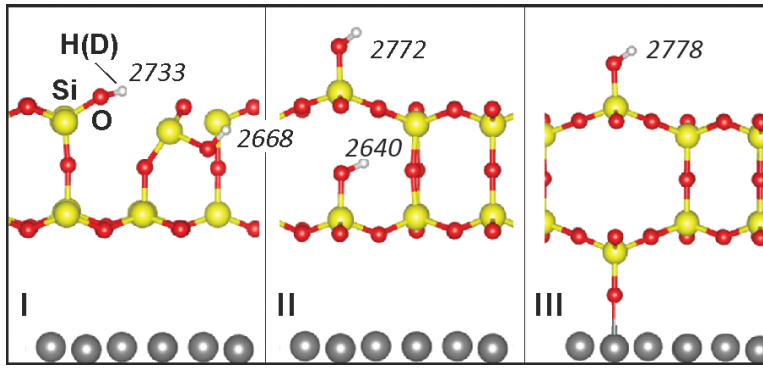

Figure 8.10 Side view of three possible structures formed upon hydroxylation of a silicate bilayer film. The DFT-computed (harmonic and scaled) frequencies for the OD stretch vibrations are shown next to hydroxyl species.

The atomic structure of the hydroxylated silicate surface was analyzed by Sauer and co-workers employing DFT calculations on a crystalline film.[19] One can anticipate several possible structures, all schematically shown in Fig. 8.10, which can be formed through breaking siloxane bonds either *in* the surface layer (structure I) or *between* the silicate layers (structure II). One more structure (III) is formed from the structure II by flipping of internal silanol towards the metal with simultaneous formation of the Si–O–Ru linkage and hydrogen migration onto the metal surface.

Actually, the relative stability of the structures depends on the amount and nature of ad-atoms adsorbed directly onto the Ru surface. If the Ru surface is covered by D atoms (that is likely based on the experimental TPD results showing large D_2 desorption signal), then structure I is most stable. Preferential breaking of the siloxane bonds in the surface plane is also consistent with the IRAS results (Fig. 8.8a) showing that the 693 cm^{-1} band, which involves bending vibrations of in plane O–Si–O bonds, is strongly suppressed, at least to a much larger extent than the high-frequency band at 1300 cm^{-1} associated with vertical Si–O–Si bonds.

The calculated (and properly scaled) frequencies are shown in Fig. 8.10 next to corresponding hydroxyl species. The terminal hydroxyls formed in structures II and III exhibit the frequencies

(2772 and 2778 cm^{-1}), which fit much better the experimentally observed 2764 cm^{-1} than the one in structure I (at 2733 cm^{-1}), albeit thermodynamically the most favorable. Note, however, that terminal hydroxyl in structure I is oriented nearly parallel to the surface and hence hardly detectable by IRAS. It seems plausible that tilted towards the surface silanol in structure I (2733 cm^{-1}) manifests itself as a weaker and broad feature (shoulder) at the low-frequency side of the principal peak at 2764 cm^{-1} (Fig. 8.8a). Second silanols formed in structures I and II are strongly red-shifted (2668 and 2640 cm^{-1}) because of hydrogen bonding to the nearest oxygen which in addition may cause band broadening. Again, these silanols are oriented parallel to the surface and hence IRAS silent. However, its presence in structure II is indirectly affirmed through its transformation into structure III at high temperatures, accompanied by release of the D atoms desorbing as D_2 in TPD spectra. In addition, the progressive formation of Si–O–Ru linkages in structure III explains why dehydroxylation of the samples by UHV annealing never recovers the original phonon spectrum of the film. Apparently, recombination of different types of hydroxyls is a stochastic process accompanied by structural transformations resulting in a complex spectral evolution of the related hydroxyl IRAS bands on heating (Fig. 8.9). Dehydroxylation of silicate films is not the reverse process of hydroxyl formation. Repeated hydroxylation over the once dehydroxylated film ultimately leads to disintegration (de-wetting) of the silica film after few cycles.

Finally, we speculate about origin of IR band splitting in above-presented isotopic experiments (Fig. 8.9). The low frequency 2746 cm^{-1} band has tentatively been assigned to $^{18}O_SD$ hydroxyl, whereas according to the DFT calculations such hydroxyls should show frequencies well below 2668 and 2640 cm^{-1} computed for "lighter" ^{16}OD species (Fig. 8.10). If, however, this band also corresponds to terminal, but ^{18}OD–Si silanol, then one should admit that ^{16}O oxygen in the water exchanges with ^{18}O oxygen in the silicate film during water $D_2^{16}O$ dissociation. One possible mechanism includes the exchange in the transition state involving both oxygens followed by rotation of the one of the two ODs resulting in the final state such that the formation of two (O_wD and O_sD) terminal hydroxyls are equally possible. Still, the precise mechanism of hydroxylation,

in particular under electron irradiation remains to be further investigated.

Among the electron beam parameters varied, ice film thickness provides the largest correlation to changes in subsequent water/hydroxyl coverage. Since almost no increase of the water/hydroxyl coverage was observed if the film thickness was in the range of one nanometer, corresponding to the inelastic mean free path the electrons, it seems that that the siloxane bonds are activated for water dissociation by water radiolysis products, e.g., hydroxyl ions, formed in the ice layer during electron bombardment.

It is worth mentioning that electron-stimulated reactions have been studied on ASW films formed on metals like Pt(111).[20] In particular, electron bombardment resulted in the evolution of molecular oxygen and hydrogen. Most likely, mobile electronic excitations (excitons) are responsible for the reactions, although the mechanism remains poorly understood. Electron irradiation of physisorbed water layer can also cause surface oxidation as demonstrated for the Si(111) surfaces irradiated with low-energy ($<$20 eV) electrons.[21] As a side note, radiation induced chemical reactions on cosmic ice dust and dust grains mainly composed of silicates may also be involved in chemical evolution in interstellar space.

8.3 Hydroxylation of Metal-Doped Silicate Films

Hydroxyls in the aluminosilicates, in particular zeolites, are probably the most important entities underlying their application in chemical industry which is primarily determined by so-called "bridging" hydroxyls, with oxygen linking the Si^{4+} and the Al^{3+} ions in the silicate framework (Si–OH_{br}–Al). Therefore, once the preparation and atomic structure of the Al-silicate films has been established (see Chapter 6), the follow-up studies were focused on the formation, identification, and adsorption properties of OH_{br} species in the films.

IRAS studies of the Ru-supported aluminosilicate films showed a band that appears at 3594 (2650) cm^{-1} upon H_2O (D_2O) adsorption. The observed frequency falls in the range typical for the bridging

hydroxyl groups measured on zeolitic systems. These bands only appear at relatively high Al:Si molar ratios in the films. The effect is explained by that Al first substitutes Si in the bottom silicate layer and only then in the topmost layer. The hydroxyls are fairly stable: The corresponding band attenuates on heating above 500 K. However, they are substantially less stable than the silanols in pure silicate films which only disappear above 900 K. OH_{br} can be replaced by OD_{br} upon exposure to D_2O and vice versa, thus indicating H–D exchange, which is also a well-known phenomenon in zeolite chemistry.

Being used as a solid acid, the important characteristic of a zeolite is their acidity, i.e., how strong is a proton bonded to the oxygen ion. Actually, measuring the acidity of zeolitic materials is not trivial.[22] A commonly used approach is based on its reaction with a weak base molecule, such as CO and ethylene. The probe molecule forms adduct with OH without breaking the O–H bond that causes a red-shift of the OH stretching frequency. This shift is believed to correlate with the ability of the proton to be transferred.

Adsorption of weak and strong bases on aluminosilicate films has been studied by IRAS. In case of CO, the spectra (see Fig. 8.11a) showed a strong red-shift for the OH stretch and a blue-shift for the CO stretch when compared to CO in the gas phase ($=2143\ cm^{-1}$), both shifts indicating CO coordination to OH. Such large shifts, about 380 and 245 cm^{-1} for ν(OH) and ν(OD) bands, respectively, and about 40 cm^{-1} for the ν(CO) band point out a high acidity of the prepared Al-silicate film surfaces, which is even comparable with the most acidic zeolites known so far.

Exposure to strong bases, such as ammonia NH_3 and pyridine C_5H_5N, even leads to a full transfer of acidic proton to the base, ultimately forming NH_4^+ and $C_5H_5NH^+$ surface ions, respectively. This is illustrated in Fig. 8.11b for the case of ammonia. The ammonium ion is located above the center of the hexagon, with three H atoms pointing toward the surface forming H-bonds to the O atoms in the topmost layer. There are two vibrational modes of NH_4^+ with strong components perpendicular to the surface plane in this configuration: A N–H stretch for the H pointing outward from the surface, and an “umbrella” mode of other three H atoms vibrating as one against N. The good match between experi-

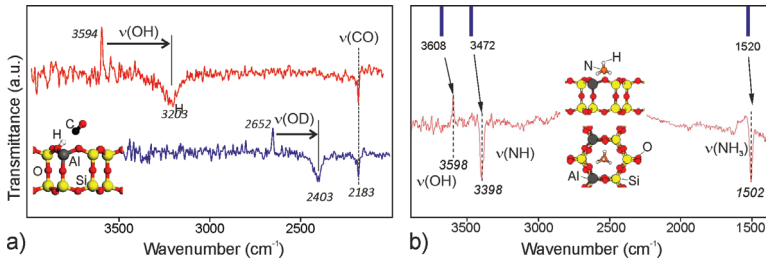

Figure 8.11 (a) IRAS spectra of the hydroxylated (OH- and OD-) aluminosilicate films grown on Ru(0001) recorded in 2×10^{-5} mbar of CO. (b) Spectrum of NH_3 adsorbed on a OH-exposing aluminosilicate film. Side and top views of DFT-optimized, free-standing bilayer model are shown in inset. The DFT-computed (scaled) frequencies for corresponding bands are presented as vertical bars. In both panels (a) and (b), each spectrum is divided by a spectrum taken before gas exposure. The positive transmittance shows the corresponding band disappearing upon the adduct formation. Adapted with permission from refs. 23, 24.

mental and theoretical values supports the proposed adsorption structure.

The adsorption characteristics of the metal-supported hydroxylated Al-silicate films fit well into what is known about zeolite surfaces. Therefore, such films may be considered as well-defined model systems to study the chemistry of zeolites using surface-science tools.

Another example is water adsorption on Fe-silicate films. It turned out that hydroxylation reaction bears close similarities to that of pure silicate films. This is not surprising since the topmost layers in both, pure and Fe-silicate, films are virtually identical (Chapter 6). As far as mixed Fe–Al-silicate films are concerned, IRAS measurements only showed a weak band at 2764 cm^{-1} which can straightforwardly be assigned to terminal silanols.[25] Also STM images of the hydroxylated films revealed atomic size features which can be assigned to isolated hydroxyls located on top of the Si atoms in full agreement with IRAS data. Interestingly, these hydroxyls are only found on the Fe-silicate domains present in the films. To date, no signature for the presence of Si–OH–Fe linkages in such films has been found, which would resemble bridging hydroxyls sometimes reported for Fe-containing zeolites.

References

1. Thiel, P. A., and T. E. Madey, The interaction of water with solid surfaces: Fundamental aspects. *Surface Science Reports*, 1987. **7**(6–8): pp. 211–385.
2. Henderson, M. A., The interaction of water with solid surfaces: Fundamental aspects revisited. *Surface Science Reports*, 2002. **46**(1–8): pp. 1–308.
3. Zhuravlev, L. T., The surface chemistry of amorphous silica. Zhuravlev model. *Colloids and Surfaces A: Physicochemical and Engineering Aspects*, 2000. **173**(1–3): pp. 1–38.
4. Rimola, A., et al., Silica surface features and their role in the adsorption of biomolecules: Computational modeling and experiments. *Chemical Reviews*, 2013. **113**(6): pp. 4216–4313.
5. de Leeuw, N. H., F. M. Higgins, and S. C. Parker, Modeling the surface structure and stability of α-quartz. *The Journal of Physical Chemistry B*, 1999. **103**(8): pp. 1270–1277.
6. Chen, Y.-W., et al., Water thin film-silica interaction on alpha-quartz (0001) surfaces. *Physical Review B*, 2011. **84**(15): p. 155444.
7. Rozanska, X., F. Delbecq, and P. Sautet, Reconstruction and stability of β-cristobalite 001, 101, and 111 surfaces during dehydroxylation. *Physical Chemistry Chemical Physics*, 2010. **12**(45): pp. 14930–14940.
8. Odelius, M., M. Bernasconi, and M. Parrinello, Two dimensional ice adsorbed on mica surface. *Physical Review Letters*, 1997. **78**(14): pp. 2855–2858.
9. Hu, J., et al., Imaging the condensation and evaporation of molecularly thin films of water with nanometer resolution. *Science*, 1995. **268**(5208): pp. 267–269.
10. Yamamoto, S., et al., Surface structure of natural crystals of mordenite as imaged by atomic force microscopy. *Chemical Physics Letters*, 1996. **260**(1): pp. 208–214.
11. Wendt, S., et al., The interaction of water with silica thin films grown on Mo(112). *Surface Science*, 2004. **565**(2–3): pp. 107–120.
12. Kaya, S., et al., Formation of an ordered ice layer on a thin silica film. *The Journal of Physical Chemistry C*, 2006. **111**(2): pp. 759–764.
13. Bensebaa, F., and T. H. Ellis, Water at surfaces: What can we learn from vibrational spectroscopy? *Progress in Surface Science*, 1995. **50**(1): pp. 173–185.

14. Michaelides, A., and K. Morgenstern, Ice nanoclusters at hydrophobic metal surfaces. *Nature Materials*, 2007. **6**: p. 597.
15. Maier, S., et al., Growth and structure of the first layers of ice on Ru(0001) and Pt(111). *Journal of the American Chemical Society*, 2016. **138**(9): pp. 3145–3151.
16. Tosoni, S., B. Civalleri, and P. Ugliengo, Hydrophobic behavior of dehydroxylated silica surfaces: A B3LYP periodic study. *The Journal of Physical Chemistry C*, 2010. **114**(47): pp. 19984–19992.
17. Yang, B., S. Shaikhutdinov, and H.-J. Freund, Tuning spatial distribution of surface hydroxyls on a metal-supported single-layer silica. *The Journal of Physical Chemistry Letters*, 2014. **5**(10): pp. 1701–1704.
18. Yang, B., et al., Hydroxylation of metal-supported sheet-like silica films. *The Journal of Physical Chemistry C*, 2013. **117**(16): pp. 8336–8344.
19. Yu, X., et al., Electron stimulated hydroxylation of a metal supported silicate film. *Physical Chemistry Chemical Physics*, 2016. **18**(5): pp. 3755–3764.
20. Smith, R. S., et al., Thermal and nonthermal physiochemical processes in nanoscale films of amorphous solid water. *Accounts of Chemical Research*, 2011. **45**(1): pp. 33–42.
21. Klyachko, D., P. Rowntree, and L. Sanche, Oxidation of hydrogen-passivated silicon surfaces induced by dissociative electron attachment to physisorbed H_2O. *Surface Science*, 1996. **346**(1–3): pp. L49–L54.
22. Bordiga, S., et al., Probing zeolites by vibrational spectroscopies. *Chemical Society Reviews*, 2015. **44**(20): pp. 7262–7341.
23. Boscoboinik, J. A., et al., Modeling zeolites with metal-supported two-dimensional aluminosilicate films. *Angewandte Chemie International Edition*, 2012. **51**(24): pp. 6005–6008.
24. Boscoboinik, J. A., et al., Interaction of probe molecules with bridging hydroxyls of two-dimensional zeolites: A surface science approach. *The Journal of Physical Chemistry C*, 2013. **117**(26): pp. 13547–13556.
25. Tissot, H., et al., Preparation and structure of Fe-containing aluminosilicate thin films. *Physical Chemistry Chemical Physics*, 2016. **18**(36): pp. 25027–25035.

Chapter 9

Silicatene *una* Graphene

Single-layer materials have recently received enormous attention owing to their two-dimensional (2D) character leading to peculiar physical and chemical properties very different from or even missing in their three-dimensional (3D) counterparts. The most famous one—graphene[1]—triggered a quest for other truly 2D materials. In fact, free-standing single layers of Si and Ge had been predicted on theoretical grounds a while ago.[2] Later they were discovered experimentally, so far only supported on metal substrates, and received the names "silicene" and "germanene," respectively.[3–6] The studies have been extended to a Sn single layer called "stanene."[7] Note, however, that possible incorporation and mixing with substrate atoms in these layers remains the subject of debate.[8,9]

From purely a geometrical point of view, the silicate layer discussed in the previous chapters may be viewed as graphene composed of SiO_4 entities instead of the C atoms. Even the defect structures in silicate layers bear close similarities to those observed on graphene. Solely on this ground, the single silicate layer merits its place in the growing family of 2D materials and as such be named "silicatene" in the same manner as for other analogs of graphene, albeit the suffix "-ene" used for such materials is somewhat

Introduction to Ultrathin Silica Films: Silicatene and Others
Shamil Shaikhutdinov

ISBN 978-981-4877-28-2 (Hardcover), 978-1-003-08862-2 (eBook)
www.jennystanford.com

confusing as it implies compounds having double bonds, according to the IUPAC's (International Union of Pure and Applied Chemistry) standards and regulations. Structural diversity of silicatene and differences compared to single layers of individual element can reasonably be attributed to the relatively high flexibility of the Si–O bonds constituting a SiO_4 unit, thus providing additional degree of freedom. This latter may explain why periodic defect structures theoretically predicted for graphene were not yet found on graphene and related carbon nanomaterials, but were observed on silicatene.

Similar to silicene and germanene, silicatene does not exist as a free-standing layer and needs a suitable substrate to coordinate otherwise unsaturated O atom out of four in SiO_4 tetrahedra. Its bonding to the metal surface can be strong, as in case of Mo and other 3d-metals, or relatively weak, as on Ru and Pd. In the bilayer film, the two silicatene layers are linked together via Si–O–Si bridges thus forming a mirror plane, and all Si–O bonds are saturated.

Inspired by potential applications of single-layer materials in nanotechnologies, one might even think about combining graphene and silicatene, for example, in sandwich-like structures which could potentially result in interesting, yet unknown functional properties of such composites. According to the theoretical calculations,[10] graphene does not form covalent bonds with a bilayer silicatene, albeit shows some stabilizing effects on its structure.

Actually, interaction of graphene with silica has only recently received attention in the course of fabrication and development of graphene-based electronic devices (in which silica is a common gate dielectric). In the early studies, silica has been used solely as a support for the optical visualization and investigation of graphene layers themselves. There were few attempts to elucidate the structure of graphene on SiO_2 with atomic resolution.[11] Thin graphite flakes were deposited using the mechanical exfoliation ("rubbing") technique on thermally grown SiO_2 films about 300 nm in the thickness. For imaging with an STM microscope integrated into standard electron microscope for coarse positioning, the e-beam lithography was used for electrodes deposition. It has turned, however, that the uncontrollable residue remains covering all graphene devices fabricated using the conventional photoresist process. The residue could only be removed by prolonged annealing

in H_2/Ar atmosphere. It was concluded that the graphene corrugation, which is relevant for interpreting of device performance, is largely due to partial conformation of the graphene to the SiO_2. The latter finding was further supported by comparative STM studies of graphene on *h*-BN and SiO_2 substrates which revealed a much smoother surface corrugation on *h*-BN because of the graphene conforming to the atomically flat surface of *h*-BN.[12] It is believed that the surface roughness may be critical for graphene-based devices because local curvature can alter electronic properties. Some experimental results pointed out that the morphology of a substrate plays a crucial role in the extrinsic strain-induced disorder in graphene and its effect on the transport properties.[13] Accordingly, the nanoscale transport properties of graphene may, to some extent, be controlled by substrate morphology. Therefore, it is not straightforward that unique physical properties of graphene persist on supported systems. In addition, they may alter under ambient atmosphere.

The interaction between graphene and SiO_2 has also been studied quite intensively by density functional theory (DFT), although the results may deviate depending on the structural models and the DFT level used.[14] Not surprisingly, the electronic structure of graphene on silica depends on the SiO_2 surface structure. The interface structures computed for some surface terminations are depicted in Fig. 9.1. Surface dangling bonds mediate the coupling to graphene and can induce hole or electron doping via charge transfer even in the absence of extrinsic impurities in SiO_2. In an interface geometry, where graphene is weakly bonded to an O-terminated silica surface, graphene is *p*-doped, whereas *n*-doping takes place on a Si-terminated surface.

A more recent DFT study[15] used α-quartz and cristobalite derived surface structures to systematically examine the interaction of graphene with several surfaces, namely: the Si-polar surface with two dangling bonds per surface Si atom, the Si-polar surface with one dangling bond per surface Si atom, the O-polar surface, the Si-adsorbed surface, the O-adsorbed surface, the reconstructed O-polar surface, and also a surface with defects. The interaction between the graphene and the silica surfaces is weak and dominated by dispersive forces which do not break the band structure of

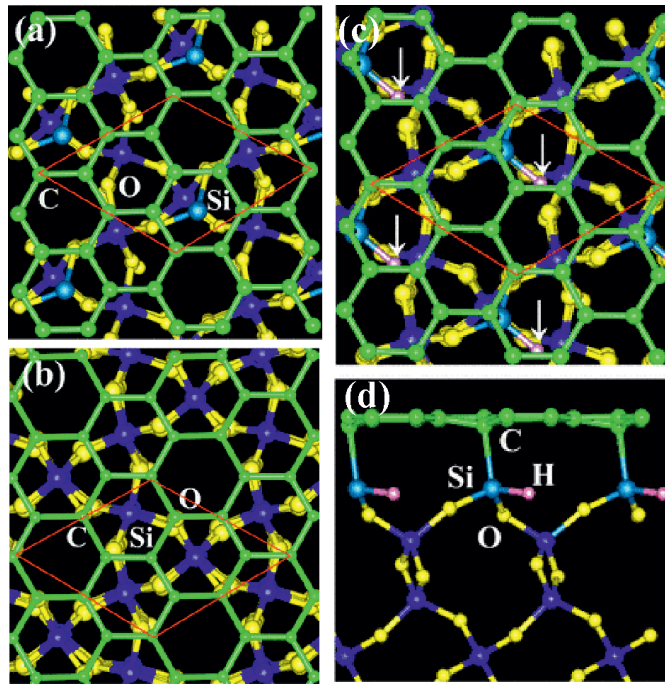

Figure 9.1 Top view of a single graphene layer on (a) Si-terminated and (b) O-terminated SiO_2 surfaces. Top (c) and side (d) views of graphene on the partially hydrogenated Si-terminated SiO_2 surface. The red lines represent the (2×2) graphene unit cell. Adapted with permission from ref. 14.

the graphene. The graphene layer keeps its planar hexagonal network. The binding energy to the Si-polar surfaces is smaller than that for the O-polar surface. H-passivated surfaces do not affect the electronic properties of the graphene irrespective of whether they are on the O-polar or Si-polar surfaces. Only surfaces with defects have a strong effect on the electronic properties of graphene. However, the cleaved SiO_2 can readily be reconstructed or hydroxylated (or hydrogenated) to eliminate the dangling bonds.

All these theoretical works highlight the point that the silica surface to be used as a substrate for fabrication of graphene/silica devices should be cleaved with an atomic level of flatness and passivated by hydrogen. In this respect, silicatene layer(s) may be a good option.

It is worth mentioning here a few studies addressing the interaction of graphene with Si ad-atoms. It appears that Si vapor-deposited onto graphene grown on a SiC(000-1) single crystal rapidly diffuses to the interface on heating.[16] DFT calculations predicted an intercalation mechanism where Si migrates through point defects in graphene.[17] It has been found that the intercalated Si atoms weaken the interaction of graphene with a metal substrate, and retain its superlative properties.[18] Another intercalation mechanism includes the penetration of Si through the graphene lattice facilitated by a Si–C exchange process.[19]

The Si layer formed underneath graphene can be oxidized in oxygen ambient, forming an amorphous silica between the graphene and the metal.[20] In order to make the interfacial silica film better ordered one can use annealing at higher temperatures. However, such treatments results in graphene disappearance from the surface due to its gasification into CO and CO_2 ("burning"), most notably observed at temperatures above 850 K. To minimize and even to avoid graphene gasification, one can, in principle, reverse the preparation process by starting with a well-ordered silica film as a substrate for subsequent graphene deposition.

To recall, the preparation of graphene layer(s) on metals commonly includes segregation of carbon impurities from the metal bulk or thermal decomposition of unsaturated hydrocarbons like ethylene.[21] Since metal supports used for the silica film growth are always thoroughly cleaned prior to the Si deposition, a carbon segregation route is hardly possible. Also, adventitious carbon readily burns out in oxygen environment during the silica film preparation. Exposure of the bilayer silicatene to ethylene at UHV-compatible pressures (typically, 10^{-6} mbar) at room temperature causes no visible effects on electronic structure and vibrational characteristics monitored by x-ray photoelectron spectroscopy (XPS) and infrared reflection absorption spectroscopy (IRAS). Increasing exposure temperature to those at which graphene is usually formed on pure metals, results in partial decomposition of the silica film accompanied by the substantial formation of reduced silica (Si^{+}) species. If the sample is exposed to elevated pressures of ethylene at relatively low temperatures, then substantial amounts of carbonaceous residues were found at the surface, yet not identified,

which, however, do not alter the principal film structure as judged by IRAS. If, however, this sample is vacuum-annealed at around 1000 K, i.e., in the temperature range of graphene formation on Ru(0001)), two vibrational bands are observed which are strongly shifted compared to original film, i.e., from 1300 to 1264 cm^{-1} and from 696 to 802 cm^{-1}, as shown in Fig. 9.1a. The intensity of new bands depends on the ethylene exposure: the bands gain in intensity at the expense of the initial bands which attenuate and ultimately disappear. Such a spectral evolution has previously been observed on the films modified by 3d-metals (see Chapter 6) and suggests the formation of two coexisting structures until the new structure covers the entire surface. Interestingly, the resulted film becomes well-ordered (see low-energy electron diffraction (LEED) pattern in Fig. 9.2a) regardless of whether the original film was fully amorphous or partially crystalline. In good agreement with LEED, the scanning tunneling microscopy (STM) images (displayed in Fig. 9.2b) show domains with a honeycomb-like structure having a ∼5.5 Å periodicity, like in the crystalline silicatene, which are separated by line defects typical for domain boundaries in hexagonal lattices.

Final piece of information came from XPS measurements (Fig. 9.2c) showing that the amount of oxygen in C-modified films decreases by a factor of 2, and no more O ad-atoms remain adsorbed onto Ru, whereas the amount of Si remains the same in total, but splits in two, almost equally populated states. The high binding energy (BE) signal at around 104 eV is shifted by about 1 eV from the one measured before the treatment. However, such a shift is also observed for the O 1s level, suggesting that it has the same origin as previously found for gas adsorption at the silica/metal interface and attributed to the band re-alignment (Chapter 7). Therefore, the high BE state can safely be assigned to the Si ions only having bonds to oxygen. Accordingly, the low BE signal at 101 eV could be indicative of sub-stoichiometric, reduced silica phase. On the other hand, it is close to the values reported for silicon carbides.[23] Therefore, the XPS results can be well explained by that about a half of oxygen ions in the film are replaced by carbon. (The carbon C 1s signal overlaps with the much stronger Ru 3d signals, and hence cannot be determined precisely.)

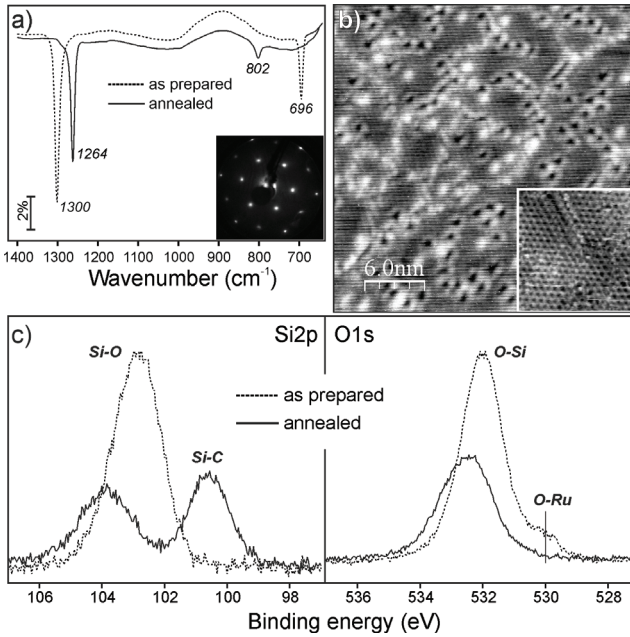

Figure 9.2 (a) Comparison of IRAS-spectra of a bilayer silicate film before (dash line) and after exposure to 10 mbar of C_2H_4 at 450 K and subsequent annealing at 1100 K in UHV (solid line). Inset shows LEED pattern demonstrating good crystallinity of the C-modified film, which is imaged by STM in panel (b). Si 2p and O 1s photoelectron spectra of the samples are shown in panel (c). Adapted with permission from ref. 22.

Random distribution of C and O atoms as well as substitution only of O atoms in the Si-O–Si interlayer linkage should result in electronically equivalent O–Si–C species and hence a single Si 2p state, which is at variance to the XPS results showing two states of Si. Accordingly, carbon only substitutes the O ions ether in the top or in the bottom silicatene layer. Taking into account that C atoms formed by ethylene decomposition only adsorb on the metal surface, carbon most likely substitutes the oxygen atoms in the bottom layer. If we further recall that silicatene layers can be formed on the SiC(0001) and (000-1) surfaces (Chapter 3), all experimental findings can be explained by the structure where a silicate layer is placed on top of a silicon carbide layer. Carbon atoms in the bottom layer most

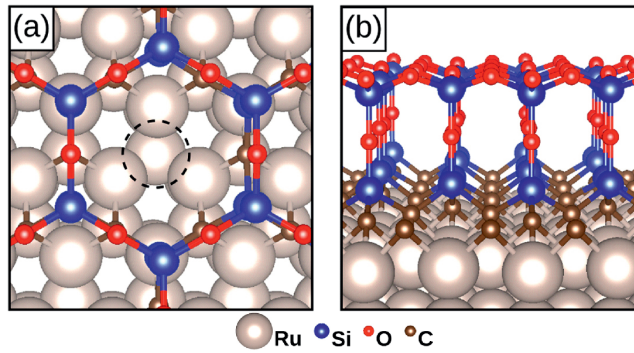

Figure 9.3 Structure of a carbon substituted silica film with a $SiC_{0.75}O_{1.25}$ composition on Ru(0001) in top (a) and side (b) views. Dashed circle indicates the Ru-hcp site. Reproduced with permission from ref. 24.

likely form strong bonds with the Ru(0001) surface, which can also explain long-range ordering in the resulted films. As we have shown before (Chapter 4), crystallinity of silicatene is primarily governed by strong interfacial bonds forcing an epitaxial relationship to a metal surface.

The proposed structure was fully supported by the DFT calculations (Fig. 9.3).[24] The adhesion energies for the silicatene/silicon-carbide film are more than one order of magnitude larger than for the pure bilayer silicatene (−510 vs. −33 meV $Å^{-2}$) due to the formation of chemical bonds to the metal surface atoms reflected in the short (2 Å) distances between C and Ru. On the basis of adhesion energies computed for various film orientations with respect to the Ru(0001) surface, the film is oriented such that the center of a silica hexagon is located over the threefold hollow site on the Ru(0001) surface as shown in Fig. 9.3a. Apparently, the hollow sites provide the best approximation for C atoms in the tetrahedral symmetry and hence indicate a preference of sp^3 hybridization over sp^2 in this system. In addition, the calculations revealed partial electron transfer from Ru to C, and also the Si atoms connected to C were less positive than the Si atoms only bonded to O.

The calculated (scaled) vibrational frequencies of IRAS active bands were compared for two systems. The principal band at 1289 cm^{-1} associated with vertical Si–O–Si bonds in the

silicatene/silicon-carbide bilayer is only 3 cm^{-1} red-shifted with respect to that of the bilayer silicatene (1292 cm^{-1}), whereas 36 cm^{-1} is found in experiment. However, the second band (at 744 cm^{-1}) is found strongly blue-shifted (by 120 cm^{-1}) with respect to the bilayer-silicatene (624 cm^{-1}), in good agreement with experiment ($\Delta\nu = 106$ cm^{-1}). The deviation from experiment may be caused by high defectness of the prepared films, as imaged by STM, whereas the calculations were carried out for perfect films.

Even though the above-described experiments have not yet been performed on other silicatene systems, it appears that the fabrication of layered graphene-silicatene structures on a metal substrate is hardly possible by synthesis based on the "intercalation" approach. Indeed, either oxidation of Si underneath graphene results in its gasification or, alternatively, annealing of carbon underneath silicatene in oxygen-free atmosphere leads to the formation of a silicon carbide layer. Although further elaborative studies have to be done to see whether silicatene/silica carbide/metal heterostructures would be potentially interesting for some applications, it appears that methods based on precipitation of graphene and silicatene "flakes" would be a more promising approach for such purposes.

In principle, the bilayer silicatene weakly binds to a metal substrate. In addition, the interface between the silica and the metal may readily be intercalated by gas molecules in the ambient. This, in turn, results in lifting of the silicate layer away from the metal surface and making the bonding even weaker. These findings allow one to believe that the films can, in principle, be stripped or exfoliated from a substrate to be further handled *à la* graphene. However, the exfoliation of bilayer silicatene remains challenging. There is only one successful approach[25] reported thus far showing transfer of the bilayer silicatene from one to another metal substrate using poly-methylmethacrylate coating, the technique also used for manipulation with graphene.

Obviously, the situation becomes even more involved for silica monolayer films having a support, which is mandatory for saturation of all the bonds in the silicate layer. This is obvious for the ideal silicate layer, where all unsaturated apical oxygen atoms are on the one side of the silicate plane. On the other hand, from topological

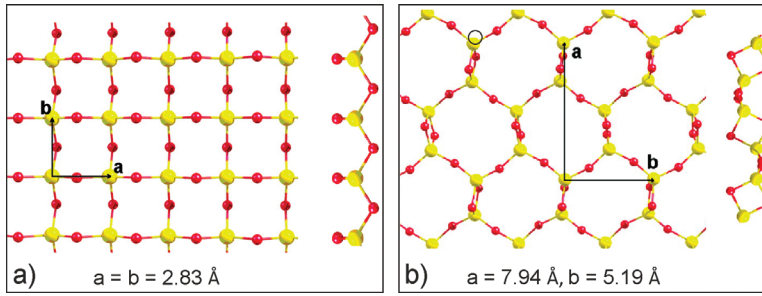

Figure 9.4 Proposed structures of 2D silica polymorphs in top and side views (**a** and **b** are the primitive translation vectors). Adapted with permission from ref. 26.

considerations and bearing in mind certain flexibility of silica bonds, it is possible to create "self-saturated" structures composed of silica tetrahedra as well as octahedra. In the lack of experimental findings, a new playground was opened up for theoreticians to search for free-standing single-layer silica structures.

Interestingly, even before substantial breakthrough in synthesis of silica monolayers on metals, Chernozatonskii analyzing nanotube structures of MO_2 dioxides proposed a "square" silica,[26,27] shown in Fig. 9.4a, which clearly differs from the hexagonal lattices commonly considered for graphene-like 2D-structures. The hypothetical nanotubes were rolled from silica monolayer showing a square unit cell with lattice constant of 2.83 Å. The Si–O bonds in this structure (1.65 Å) are somewhat stretched as compared to 1.60 Å in quartz. The Si–O–Si angle is 149° vs. 144° in quartz. However, the O–Si–O angle is by 40° larger than 109.5° in four-coordinated silica polymorphs. Therefore, bond angles around Si nuclei in this structure are quite strongly distorted. As a result, the calculated binding energy per SiO_2 unit for this "tetragonal" silica sheet is 0.75 eV higher than for quartz.

A more typical for silicas "trigonal" structure is shown in Fig. 9.4b. However, the layer has a two-membered ring in the structure. The Si–O bonds in two-membered rings are stretched to 1.67 Å, and the Si–O–Si angle is 89°, which again implies a strong deviation from tetrahedral geometry around Si nuclei. The calculated energy is 0.65 eV higher than for α-quartz.

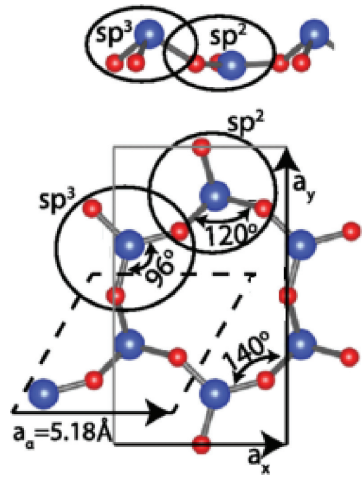

Figure 9.5 Optimized structure of *hα* silica with its hexagonal and rectangular unit cells. Two types of Si atoms, i.e., like sp^3 - and sp^2–bonded, are indicated. Reproduced with permission from ref. 28.

Another hypothetical structure, named *hα* silica, was derived from the oxidation of silicene resulting in a single silica layer with a Si_2O_3 stoichiometry having alternating sp^3- and sp^2–like bonds (Fig. 9.5). The 2D silica showed a wide band gap, a negative Poisson's ratio, and a high piezoelectric coefficient.[28] Although the layer was found thermodynamically stable, high reactivity of dangling Si bonds renders its fabrication hardly possible.

The follow-up first-principles calculations[29] examined various free-standing 2D silica monolayers with tetrahedral (*T*-silica) and octahedral (*O*-silica) building blocks. *T*-silica is formed by corner-sharing SiO_4 tetrahedra in a rectangular network, and *O*-silica consists of edge-sharing SiO_6 octahedra. *O*-silica is the first proposed 2D silica with octahedral-coordinated building blocks. The results for three 2D structures are shown in Fig. 9.6. The calculated formation energies of *O*-silica and *T*-silica are −2.77 and −2.70 eV/atom, respectively, which are very close to the value −2.82 eV/atom computed for the bilayer silicatene also shown in Fig. 9.6. For comparison, the above-mentioned *hα* silica only yielded −1.94 eV at the minimum, thus suggesting its considerably lower stability.

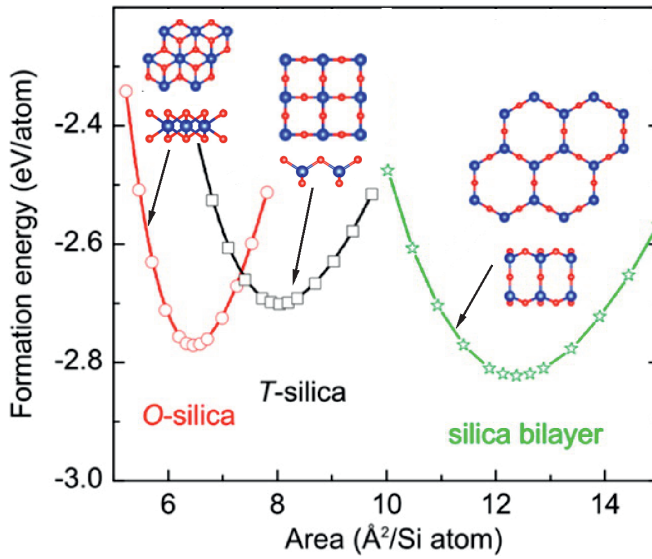

Figure 9.6 Calculated formation energy vs. area/Si atom for several 2D silica configurations schematically shown in top and side views. Large blue and small red balls in the represent silicon and oxygen atoms, respectively. Adapted with permission from ref. 29.

Considering that the sixfold-coordinated silica polymorphs (e.g., stishovite) exists at high pressure in the bulk phase, the prediction of a small energy difference of *O*-silica with the synthesized silica bilayer, together with the thermal stability at 1000 K, suggests that synthesis of *O*-silica can be achieved in experiments.

More recently, three new hypothetical 2D silica structures were reported, denoted by the authors as β-, γ-, and δ-2D silica (all shown in Fig. 9.7), from calculations using evolutionary algorithm.[30] Note, however, that the δ-2D structure, in fact, reproduces the one previously proposed (see Fig. 9.4a). All structures exhibit rectangular symmetry in the top view, and β- and γ-2D layers are strongly buckled in terms of the Si atom position in the side view, and have three different Si–O bond lengths in the structure. The calculations predicted extremely large in-plane negative Poisson's ratios in all these 2D layers. In addition, these materials are superhard, suggesting superior thermal conductivities compared

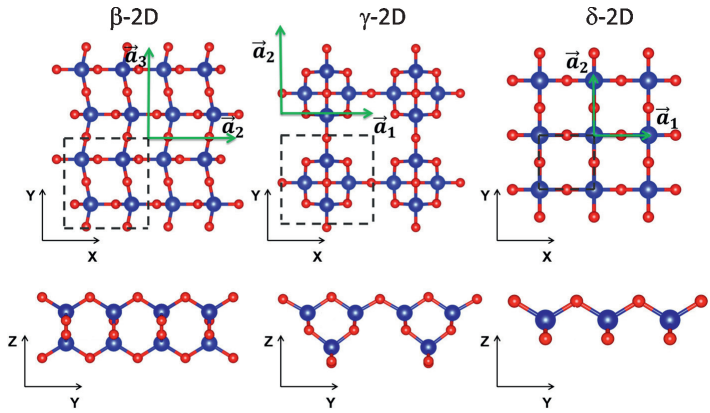

Figure 9.7 Equilibrium 2D silica structures in top and side views. Large blue and small red balls in the represent silicon and oxygen atoms, respectively. Adapted with permission from ref. 30.

to bulk silica, and exhibit large electronic band gaps as compared to other 2D materials. Such "exotic" 2D silica may find interesting applications in nanomechanics and nanoelectronics.

To sum up, a growing up body of theoretical results favors the possibility that low-energy 2D silica structures do exist in nature and can be prepared in laboratories. In principle, they all may be referred to as silicatenes, implying that they are single-layer silicas. The fact that only a few these silica structures have been experimentally identified suggests that their existence is determined by the kinetics rather than by the energetics of the final structure. It is also possible that there remain a large number of 2D silica structures yet to be discovered.

References

1. Geim, A. K., and K. S. Novoselov, The rise of graphene. *Nature Materials*, 2007. **6**(3): pp. 183–191.
2. Takeda, K., and K. Shiraishi, Theoretical possibility of stage corrugation in Si and Ge analogs of graphite. *Physical Review B*, 1994. **50**(20): pp. 14916–14922.

3. Vogt, P., et al., Silicene: Compelling experimental evidence for graphene-like two-dimensional silicon. *Physical Review Letters*, 2012. **108**(15): p. 155501.
4. Guzmán-Verri, G. G., and L. C. Lew Yan Voon, Electronic structure of silicon-based nanostructures. *Physical Review B*, 2007. **76**(7): p. 075131.
5. Dávila, M. E., et al., Germanene: A novel two-dimensional germanium allotrope akin to graphene and silicene. *New Journal of Physics*, 2014. **16**(9): p. 095002.
6. Cahangirov, S., et al., Two- and one-dimensional honeycomb structures of silicon and germanium. *Physical Review Letters*, 2009. **102**(23): p. 236804.
7. Zhu, F.-F., et al., Epitaxial growth of two-dimensional stanene. *Nature Materials*, 2015. **14**: p. 1020.
8. Cantero, E. D., et al., Growth of germanium on Au(111): Formation of germanene or intermixing of Au and Ge atoms? *Physical Chemistry Chemical Physics*, 2017. **19**(28): pp. 18580–18586.
9. Junji, Y., et al., Large area planar stanene epitaxially grown on Ag(1 1 1). *2D Materials*, 2018. **5**(2): p. 025002.
10. Huang, P. Y., et al., Direct imaging of a two-dimensional silica glass on graphene. *Nano Letters*, 2012. **12**(2): pp. 1081–1086.
11. Ishigami, M., et al., Atomic structure of graphene on SiO_2. *Nano Letters*, 2007. **7**(6): p. 1643–1648.
12. Xue, J., et al., Scanning tunnelling microscopy and spectroscopy of ultra-flat graphene on hexagonal boron nitride. *Nature Materials*, 2011. **10**: p. 282.
13. Gao, N., and X. Fang, Synthesis and development of graphene–inorganic semiconductor nanocomposites. *Chemical Reviews*, 2015. **115**(16): pp. 8294–8343.
14. Kang, Y.-J., J. Kang, and K. J. Chang, Electronic structure of graphene and doping effect on SiO_2. *Physical Review B*, 2008. **78**(11): p. 115404.
15. Fan, X. F., et al., Interaction between graphene and the surface of SiO_2. *Journal of Physics: Condensed Matter*, 2012. **24**(30): p. 305004.
16. Wang, F., et al., Silicon intercalation into the graphene-SiC interface. *Physical Review B*, 2012. **85**(16): p. 165449.
17. Kaloni, T. P., et al., Mechanism of Si intercalation in defective graphene on SiC. *Journal of Materials Chemistry*, 2012. **22**(44): pp. 23340–23343.

18. Mao, J., et al., Silicon layer intercalation of centimeter-scale, epitaxially grown monolayer graphene on Ru(0001). *Applied Physics Letters*, 2012. **100**(9): p. 093101.
19. Cui, Y., et al., An exchange intercalation mechanism for the formation of a two-dimensional Si structure underneath graphene. *Nano Research*, 2012. **5**(5): pp. 352–360.
20. Lizzit, S., et al., Transfer-free electrical insulation of epitaxial graphene from its metal substrate. *Nano Letters*, 2012. **12**(9): pp. 4503–4507.
21. Tetlow, H., et al., Growth of epitaxial graphene: Theory and experiment. *Physics Reports*, 2014. **542**(3): pp. 195–295.
22. Yang, B., S. Shaikhutdinov, and H.-J. Freund, Ultrathin silicatene/silicon-carbide hybrid film on a metal substrate. *Surface Science*, 2015. **632**(0): pp. 9–13.
23. Kusunoki, I., and Y. Igari, XPS study of a SiC film produced on Si(100) by reaction with a C_2H_2 beam. *Applied Surface Science*, 1992. **59**(2): pp. 95–104.
24. Schlexer, P., and G. Pacchioni, Modelling of an ultra-thin silicatene/silicon-carbide hybrid film. *Journal of Physics: Condensed Matter*, 2016. **28**(36): p. 364005.
25. Büchner, C., and M. Heyde, Two-dimensional silica opens new perspectives. *Progress in Surface Science*, 2017. **92**(4): pp. 341–374.
26. Artyukhov, V. I., and L. A. Chernozatonskii, Theoretical study of two-dimensional silica films. *The Journal of Physical Chemistry C*, 2010. **114**(21): pp. 9678–9684.
27. Chernozatonskii, L. A., A new class of MO_2 dioxide nanotubes (M=Si, Ge, Sn, Pb) composed of "square" lattices of atoms: Their structure and energy characteristics. *Journal of Experimental and Theoretical Physics Letters*, 2004. **80**(10): pp. 628–632.
28. Özçelik, V. O., S. Cahangirov, and S. Ciraci, Stable single-layer honeycomblike structure of silica. *Physical Review Letters*, 2014. **112**(24): p. 246803.
29. Wang, G., et al., Novel two-dimensional silica monolayers with tetrahedral and octahedral configurations. *The Journal of Physical Chemistry C*, 2015. **119**(27): pp. 15654–15660.
30. Gao, Z., et al., Novel two-dimensional silicon dioxide with in-plane negative Poisson's ratio. *Nano Letters*, 2017. **17**(2): pp. 772–777.

Index

"*This excellent and complete overview covers all aspects, from preparation to characterization and potential use, of the emerging field of two-dimensional silica and silicates. From their discovery 20 years ago as model systems for catalysis, the study of these nanostructured materials has opened up new intriguing scenarios for their potential applications as nanoscale molecular sieves, protecting layers, or to perform reactions in confined space.*"

Prof. Gianfranco Pacchioni
Universita' degli Studi di Milano-Bicocca, Italy

Silica is one of the key materials in many modern technological applications. Further miniaturization of nanoelectronic devices necessitates rational design of ultrathin silica films on electrically conductive substrates. This is the first-ever book on the preparation and atomic-level description of ultrathin silica films grown on metal substrates. Experimental and theoretical studies performed in recent years provide compelling evidence of the growth of well-ordered silica films that exhibit the structural motif of sheet silicates. A growing body of research suggests that a single-layer silicate, which received the name *silicatene* by analogy with the famous graphene, should be included in the family of truly two-dimensional materials. In addition, the silicate films modified with metals such as Al and Fe offer a unique possibility to study the surface structures (and hence the surface chemistry) of natural silicates, e.g., clays and zeolites. Finally, ultrathin silica films represent well-defined model systems for elucidating the mechanism of crystal–glass transitions.

Shamil Shaikhutdinov received his PhD in physics in 1986 from the Moscow Institute of Physics and Technology for the study of microwave dielectric properties of inorganic materials. Then he joined the Boreskov Institute of Catalysis at Novosibirsk to carry out "surface science" studies of catalytic systems, in particular with scanning tunneling microscopy. Since 2004, he is leading the "Structure and Reactivity" group at the Fritz-Haber Institute at Berlin. His research interests focus on the fundamental understanding of atomic structures and surface chemistry of functional materials based on ultrathin films.

V786
ISBN 978-981-4877-28-2
9 789814 877282

Jenny Stanford
Publishing